



PONTIFICIA UNIVERSIDAD CATOLICA DE CHILE
ESCUELA DE INGENIERIA

**EFFECT OF SCANNING DIRECTION,
ATMOSPHERIC OXYGEN AND LASER POWER
ON MECHANICAL PROPERTIES OF
SELECTIVE LASER SINTERING (SLS) OF
ALUMINUM-FILLED POLYAMIDE
MONOLAYERS**

FERNANDO JOSE ALAMOS DOMEYKO

Thesis submitted to the Office of Research and Graduate Studies in partial fulfillment of the requirements for the Degree of Master of Science in Engineering

Advisor:

DR. JORGE RAMOS GREZ

Santiago de Chile, October, 2018

© MMXVIII, Fernando José Alamos Domeyko



PONTIFICIA UNIVERSIDAD CATOLICA DE CHILE
ESCUELA DE INGENIERIA

**EFFECT OF SCANNING DIRECTION,
ATMOSPHERIC OXYGEN AND LASER POWER
ON MECHANICAL PROPERTIES OF
SELECTIVE LASER SINTERING (SLS) OF
ALUMINUM-FILLED POLYAMIDE
MONOLAYERS**

FERNANDO JOSE ALAMOS DOMEYKO

Members of the Committee:

JORGE RAMOS GREZ

LORETO M. VALENZUELA

STEVEN R. SCHMID 

MARCOS SEPÚLVEDA FERNÁNDEZ

Thesis submitted to the Office of Research and Graduate Studies in partial fulfillment of the requirements for the Degree of Master of Science in Engineering

Santiago de Chile, October, 2018

To God, my Parents, siblings and friends, who supported me and gave me the strength to accomplish this dream.

ACKNOWLEDGMENTS

First, I am grateful to God for giving me the strength and perseverance to accomplish this mechanical engineer master degree.

I would like to express my deepest appreciation to my adviser Jorge Ramos and his invaluable edification and guidance during graduate school and life. Without his encouragement and enlightenment, this dream would have been impossible. I have enjoyed working with him, especially because of his always positive attitude, constant help, and support.

Also, I take this opportunity to express gratitude to all the members of the mechanical department for their help and support, specially to Patricio Pérez for his help and supervision during the tensile testing, to Luis Valdés, Marcelo, and Miguel Ángel for their advice and help during the experiment.

I would like to thanks to the UND-PUC Seed Fund for supporting the SEM, EDS electronic microscope analysis.

My sincerest appreciations go to Dr. Steven Schmid and Dr. Glen Neibur, who helped me to finish this thesis at the University of Notre Dame, with the access to the Micro CT and different labs.

Finally, special thanks to my parents, siblings, and friends, who played a key role on my studies and life with their constant and unconditional help. Without your support behind me, I would never be able to accomplish this master degree and dreams.

TABLE OF CONTENTS

ACKNOWLEDGMENTS	ii
LIST OF TABLES	v
LIST OF FIGURES	vi
ABSTRACT	ix
RESUMEN.....	x
1. Scientific Background	1
1.1. Introduction	1
1.2. Motivation	3
1.3. Hypothesis.....	4
1.4. Main Goals	4
1.5. Literature Review	5
1.5.1. Selective Laser Sintering	5
1.5.2. SLS Printing Parameters.....	6
1.5.3. Consolidation Phenomena	9
1.5.4. Energy Diffusion in SLS	13
1.5.5. Design of Experiment	14
1.6. Preliminary Investigation	15
1.6.1. Material and methodology	15
1.6.2. Results and discussion	15
1.6.3. Conclusion	17
2. Main Article: Effect of scanning direction, atmospheric oxygen and laser power on mechanical properties of selective laser sintering (SLS) of aluminum-filled polyamide monolayers.....	18
2.1. Abstract	18
2.2. Introduction	18
2.3. Experimental Procedure	21
2.3.1. SLS Set-up and Material.....	22
2.3.2. Fabrication Procedure	23
2.3.3. Characterization and Calibration	25

2.3.4. Analysis of the Design of Experiment.....	27
2.4. Results and Discussion.....	27
2.4.1. Tensile Testing.....	27
2.4.2. Delay Time	32
2.4.3. Specimen Thickness	33
2.5.3. Density and Porosity.....	35
2.5.4. Optimized Response	37
2.5.5. Morphology	39
2.4.4. Microtomography	45
2.5. Conclusions	48
2.6. Further Research	49
REFERENCES.....	51
A p p e n d i x.....	54
A. Stress-strain curves from tensile testing	55
B. Descriptive statistic for the responses.....	56
C. ANOVA test residuals plots	59
D. Regresion equations.....	61
E. SEM Micrographs.....	63
F. Micro CT analysis.....	69

LIST OF TABLES

Table 2-1: Properties of Alumide powder (EOS GmbH, 2012).....	23
Table 2-2: Fixed printed parameters.	24
Table 2-3: Ultimate tensile strength ANOVA test results.	31
Table 2-4: Elongation at fracture ANOVA test results.....	32
Table 2-5: Specimen thickness ANOVA test results.....	35
Table 2-6: Density ANOVA test results.	37
Table 2-7: Optimum parameters of the experiment.	38
Table 2-8: Predicted optimized response compared with experimental results and EOS MDS values (EOS GmbH, 2012).....	38
Table B-1: Results of means and standard deviations (SD) for UTS and elongation.....	56
Table B-2: Results of means and standard deviations (SD) for density and specimen thickness.....	57
Table B-3: Results of the porosity analysis.....	58

LIST OF FIGURES

Figure 1-1: Rapid prototype machine saleswide (Wohler, 2001).	1
Figure 1-2: Selective laser sintering schematics (Hopkinson et al., 2005).	6
Figure 1-3: SLS printed parameters schematic (Negi et al., 2015).	7
Figure 1-4: Tensile strength at various orientations based on delay time for EOS PA 2200 bars (Jain et al., 2009).	8
Figure 1-5: Yellowish discoloration of the material measured at different temperatures and oxygen levels (Kummert et al., 2017).	9
Figure 1-6: Sintering process. (a) Particles prior to sintering. (b) Particles start to agglomerate creating necks between them. (c) Neck size increase and pore size decrease during the sintering (Gibson et al., 2015).	10
Figure 1-7: Sintering phase of composite powder material (Eisen et al., 1998).	11
Figure 1-8. Different materials used in liquid phase sintering. (a) Mixture of two- component powder. (b) Composite powder particles. (c) Coated particles. (d) Indistinct mixture. The black regions are the binder material and the light regions are the structural material (Gibson et al., 2015).	11
Figure 1-9: Main energy terms in the meltpool (Franco et al., 2010).	14
Figure 1-10: Isotherms causes by a linear source in the powder bed (Franco et al., 2010).	14
Figure 1-11: (a) Micrograph of the analyzed particle. (b) EDS analysis of a PA-12 particle.	16
Figure 1-12: (a) Micrograph of the analyzed particle. (b) EDS analysis of an aluminum particle.	17
Figure 2-1: Experimental set-up schematic.	22
Figure 2-2: Chamber used to fabricate the specimens.	23
Figure 2-3: Scanning direction angles (0°, 45°, and 60°).	24

Figure 2-4: Stress(σ)-strain (ϵ) curves for specimens printed at 11 W and nominal atmospheric conditions at 0°, 45° and 60° .	28
Figure 2-5: Ultimate tensile strength (a) and elongation (b) versus scanning direction angle.	29
Figure 2-6: (a) Main effect plots, and (b) interactions plots for UTS.	30
Figure 2-7: (a) Main effect plots, and (b) interactions plots for elongation.	31
Figure 2-8: UTS results versus delay time.	33
Figure 2-9: Specimen thickness versus scanning direction angle.	34
Figure 2-10: (a) Main effect plots, and (b) interactions plots for specimen thickness.	35
Figure 2-11: (a) Density versus scanning angle plots. (b) Porosity versus scanning angle plots.	36
Figure 2-12: Optimization plot maximizing the UTS, elongation, and density responses.	38
Figure 2-13: SEM images of Alumide powder. (a) Virgin powder sample (250x). (b) PA-12 particle (2500x). (c) Aluminum particle (2000x).	40
Figure 2-14: Micrographs at the fractured surface. (a) Overall view of a specimen printed at 11 W, 21% oxygen, and 0° showing a ductile and a fragile fracture zones (250x). (b) Top area of a specimen printed at 11 W, 0.5% oxygen, and 0° (500x). (c) Ductile fracture zone at the middle of the specimens of specimen printed at 11 W, 0.5% oxygen, and 0° (1000x). (d) Fragile fracture zone at the top of a specimen printed at 11 W, 21% oxygen, and 0° (1000x).	42
Figure 2-15: Micrographs of the top surface of the specimens. (a) Overall view of a specimen printed at 10 W, 21% oxygen, and 60° (250x). (b) Amplification of the spherulites formed on the polyamide matrix having a diameter near to 10 μm (5000x).	43
Figure 2-16: Micrographs of the bottom surface of the specimens. (a) Overall view of a specimen printed at 11 W, 21% oxygen, and 60° (250x). (b) Amplification of the image (1000x).	44

Figure 2-17: Micrograph at the bottom area of the fractured surface. An unmelted PA-12 particle is adhered and surrounded by melted PA-12 (8000x)..... 44

Figure 2-18: Micro CT cross-section images. (a) Specimen printed at 10 W, 21% oxygen, and 60°. (b) Phantom evaluation of the specimen printed at 10 W, 21% oxygen, and 60°. (c) Specimen printed at 10 W, 0.5% oxygen, and 60°. (d) Phantom evaluation of the specimen printed at 10 W, 0.5% oxygen, and 60°..... 46

Figure 2-19: 3-D Micro CT images of specimens at 11 W and 0.5% oxygen with different scanning angles. (a) Full specimen. (b) Analyzed volume of a specimen printed at 0°, (c) at 45°, and (d) at 60°. 47

Figure C-1: Residuals plots for ultimate tensile strength..... 59

Figure C-2: Residuals plots for elongation. 59

Figure C-3: Residuals plots for specimen thickness. 60

Figure C-4: Residuals plots for density..... 60

ABSTRACT

In selective laser sintering (SLS) the quality and mechanicals properties of the final printed parts depend strongly on the printing parameters. Therefore, the purposes of this thesis are 1) to study the influence of scanning direction, atmospheric oxygen, and laser power on five responses: ultimate tensile strength (UTS), elongation at fracture, density, porosity, and layer thickness, and 2) to investigate the morphology and joint mechanism of laser-sintered aluminum-filled polyamide-12 (EOS Alumide) monolayer specimens.

The scanning angle, oxygen level, and laser power were the manipulated factors of a design of experiment (DOE) with three replicates. Tensile testing, measurement of densities and dimensions, a scanning electron microscopy (SEM), an energy dispersive X-ray spectroscopy (EDS), and a Micro CT were used to characterize the specimens.

The results show that a higher scanning angle and higher laser power significantly increase the UTS, elongation, and layer thickness. However, the oxygen level only has a small effect on the elongation to fracture and on the other properties when combined with laser power or scanning angle. No changes in the morphology and internal structure in the specimens were observed using different sets of parameters. The morphology analysis revealed a composite structure formed by Al particles submerged in a molten polyamide matrix, where failure occurs at the polyamide. Two failure mechanisms were observed: a ductile failure that occurs when the particles are well-blended because the Al particles work effectively by obstructing crack propagations, and a fragile failure when the amount of Al particles is poor.

As a conclusion, the laser beam has strong influence in SLS products. The scan path creates anisotropic parts, and the energy density has a significant effect on the mechanical properties. Additionally, oxidation and degradation of the material only have a small effect on the elongation to fracture of the specimens.

Keywords: Polyamide, aluminum, composite material, additive manufacturing, selective laser sintering, mechanical properties, anisotropy.

RESUMEN

Los parámetros de impresión utilizados en el sintetizado láser selectivo (SLS) tienen un alto impacto en la calidad y propiedades mecánicas de los productos fabricados por este método. Por lo tanto, los propósitos de esta tesis son 1) estudiar el efecto del nivel de oxígeno, ángulo de escaneo y potencia del láser en cinco respuestas: resistencia última (UTS), elongación de fractura, densidad, porosidad y espesor de capa, y 2) investigar la morfología y mecanismos de adhesión de monocapas de aluminio y poliamida 12 (EOS Alumide) sintetizadas por láser.

El ángulo de escaneo, nivel de oxígeno y potencia del láser fueron los factores en un diseño experimental (DOE) con tres réplicas. Para caracterizar las probetas fueron utilizados ensayos de tracción, medición de densidades y dimensiones, un microscopio electrónico (SEM), un espectrómetro de rayos X de energía dispersiva y un micro CT.

Los resultados revelan un significativo aumento en UTS, elongación y espesor de capa para un ángulo de escaneo más amplio y mayor potencia del láser. Sin embargo, el nivel de oxígeno solamente causa un pequeño efecto en las propiedades cuando es combinado con la potencia del láser o el ángulo de escaneo. No se observaron efectos significativos en la morfología y estructura interna entre los diferentes parámetros. El análisis reveló una estructura compuesta formada por partículas de aluminio sumergidas en una matriz de poliamida fundida, donde la fractura ocurre en la poliamida. Dos mecanismos de fractura fueron observados: fractura dúctil en las zonas donde las partículas están bien mezcladas, debido a que las partículas de aluminio obstruyen las propagaciones de grietas, y fractura frágil cuando la cantidad de partículas de aluminio es escasa.

En conclusión, las piezas fabricadas por SLS son altamente influenciadas por el láser. La trayectoria del láser genera piezas con anisotropía y densidad energética tiene un efecto significativo en las propiedades mecánicas. Adicionalmente, la oxidación y degradación del material solo tiene un pequeño efecto en la elongación hasta la fractura de las probetas.

Palabras claves: poliamida, aluminio, material compuesto, manufactura aditiva, sintetizado de láser selectivo, propiedades mecánicas, anisotropía.

1. SCIENTIFIC BACKGROUND

1.1. Introduction

Additive manufacturing (AM) operations can build parts by layers, allowing the fabrication of complex 3D-shaped parts. There are a variety of this processes such as, stereolithography, three-dimensional printing, selective laser sintering (SLS), electron-beam melting, and fused-deposition modeling (Kalpakjian & Schmid, 2014). One of the first commercialized AM process was SLS, developed in 1986 at the University of Texas, USA (Gibson et al., 2015). Sales took off exponentially after 1994 (Figure 1-1) and have been growing until today. The SLS process builds 3-D objects by selectively fusing together successive layers of powdered material. First, a 3-D CAD model (computer aided design) is sliced into discrete layers by a software. Second, a thin layer of powder from the supply chamber is spread over the powder bed area, usually the thickness of this layer is in order of microns which depends on the powder particle size. Third, a computer-controlled laser beam scans the cross-section area of the corresponding layer, heating and sintering the powder particles. This process is repeated multiple times until all layers are built, generating a 3-D object.

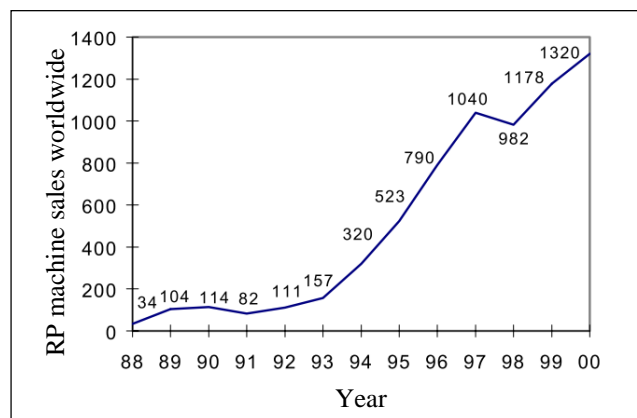


Figure 1-1: Rapid prototype machine saleswide (Wohler, 2001).

Additive manufacturing allows the construction of complex prototypes and reduces the number of tools and machines that are usually needed; this, in turn, considerably reduces

the time and cost of fabricating prototypes and consequently accelerates the design process. Therefore, AM is also called rapid prototyping (RP) or rapid manufacturing. This is one of the most important advantages of AM, which has significantly contributed to the growth of this technology in the last decades. Today SLS applications are growing, and it is extensively used in many different industries such as automobile, aeronautics, biomedical, artistic and customer consumer products (Negi et al., 2013), (Negi et al., 2014). The main advantages of SLS are the variety of materials that can be used, including a wide range of polymers (i.e. ABS, PVC, polyester, polyamide, nylon, polystyrene, and epoxy), wax, metals, ceramics, and numerous types of composites (Kalpakjian & Schmid, 2014). Polymers are most commonly used because they are less expensive and not too complicated to sinter with a laser. Also, SLS does not usually require support structures, is a fully automatic process, is a speedy fabrication process in comparison with other technologies, and has an easy post-processing treatment (Steen & Mazumder, 2010), (Negi et al., 2015). Nevertheless, SLS has significant limitations. SLS parts have lower tensile strength, lower tensile modulus, lower elongation properties, and a shorter service life in comparison with conventional processing techniques, such as injection molding for polymers and machining for metals.

Composites materials can be use in SLS. The inclusion of fillers usually improves the mechanical properties of polymers, maintaining their light weight and ductile nature. Therefore, composite materials are used in the polymer industry on specific applications, especially when stiff and strong parts are required. Nonetheless, the properties of laser-sintered parts also depend significantly on the printing SLS parameters such as bed temperature, laser power, scan speed, scan spacing, scan count, layer thickness and delay time (Goodridge et al., 2012). In this thesis, an aluminum-filled polyamide composite material was laser-sintered to print monolayers specimens, and an analysis of the effect of different printing parameters in the mechanical properties is presented.

The rest of this thesis is structured as follow: section 1.2 explains the motivation and relevance of this research, section 1.3 states the hypothesis of the thesis, section 1.4 presents the main objectives pursued in this work, section 1.5 is a literature review of the main theoretical framework about the fundamentals physics during the sintering process,

and a description of the importance of the SLS printing parameters with a review of various studies of the effect of the scanning angle and oxygen level in the mechanical properties. Section 1.6 is a preliminary investigation of the material characterization. Section 1.7 present the conclusion of the thesis and section 1.8 recommendation for future research. Following this, chapter 2 contains the main article of this thesis, where section 2.1 presents the introduction of the article, section 2.2 contains the experimental set-up and used methodologies, section 2.3 present the obtained results and discussions, and finally section 2.5 are the conclusions of this work. The appendix includes all the stress-strain curves from tensile testing, the tables of the descriptive statistical analysis, the residual plots of responses of the DOE analysis, the regression equations obtained from the statistical analysis for each response, the SEM micrographs, and Micro CT images.

1.2. Motivation

The results of the investigation should promote the study and development of additive manufacturing in Chile, specifically in the development of composite materials. Layer manufacturing allows rapid product development and production, and its capacity to design complex 3-dimensional geometries has revolutionized the manufacturing in the world, where the sales of this technology have been growing exponentially since 1994 (Wohler, 2001), as illustrated in Figure 1-1. The composite materials for SLS can be obtained with specific functional and mechanical properties; therefore, its study is important to characterize the material and be able to design news parts, where Chile can take an important role to develop the polymer and composites industry in the country.

Additionally, the results of the research should give information of SLS parameters to print Alumide powders (EOS GmbH, 2012) and improve mechanical properties or decrease the cost of manufacturing. The anisotropy in SLS parts is a property that should be considered (Bassoli et al., 2012), (Jain et al., 2009), which is caused by the orientations of the layers and the scanning direction for each layer, and has significant effect in the mechanical properties of the parts. During the printing process, a low oxygen atmosphere is used, where nitrogen and argon are the most common gases used to displace the oxygen which is inside of the building chamber; however, the effect of atmospheric oxygen during

the fabrication process of SLS polyamide parts is not clear yet, which means, for example, that maybe the cost of the gases can be reduced during the printing without compromising the quality of the parts. So far, our literature review has not shown any previous studies about this.

SLS monolayers were printed in this thesis to study the properties of single layer bars. Multilayers objects were not studied in this research because there were not multilayer systems available in the facilities. Furthermore, the goal of the thesis is to examine the behavior and properties of a single layer instead of a bulk, to better understand the effects of SLS printing parameters and the join mechanism in an aluminum-filled polyamide composite laser-sintered layer.

1.3. Hypothesis

The printing parameters of the selective laser sintering (SLS) such as scanning direction, atmospheric oxygen and laser power have an influence on the mechanical properties of the aluminum-filled polyamide monolayers. The modification of each parameter would change the mechanical properties of the specimens.

1.4. Main Goals

The general goal of this research is to make an experimental study of the effect of atmospheric oxygen, scanning direction, energy density and other parameters of the selective laser sintering (SLS) on the microstructure and mechanical properties of aluminum-filled polyamide monolayers, and find the best printed parameters within the used rank parameters.

Furthermore, the specific goals are the following:

1. Build a chamber able to establish a control atmospheric pressure about 0.8 to 6 bars, to vary the percent of atmospheric oxygen inside of the chamber.
2. Determine and adjust the process parameters to reach the optimal sintered condition for consistent results.
3. Select and determine the windows of the process parameters to investigate their influence on the mechanical properties.

4. Build the same specimens combining the different parameters using one standard operating procedure, to ensure the repeatability and independence of the results.
5. Study and analyze the influence of the selected process parameters on the microstructure and mechanical properties of the specimens.

1.5. Literature Review

1.5.1. Selective Laser Sintering

The SLS process is a powder bed fusion (PBF) process which builds 3-D objects by melting and sintering powdered material layer by layer. SLS has different applications in various industries due to its versatility in processing a wide range of materials, where most of the materials that can melt or sinter can be used in this process. Most of the SLS machines basically consist of a thermal source which melts and sinters the powder, a chamber which contains the supply powder, a second chamber where the part is built, and a mechanism that moves the powder from the supply to the built chamber. Figure 1-2 shows the schematics of a two feed chamber SLS machine with counter rotation roller, typically use by 3D Systems.

SLS basically consists of the process described below. First, the supply chamber is raised and provides a thin layer of powder, and simultaneously the build chamber is lowered below the bed level. Then a roller or a blade is used to move and spread the powder from the supply to the built chamber, forming a thin layer of powder, typically between 20 to 150 μm , depending the particle size of the powder. After the powder is spread, a laser beam is used to scan and melt the unfused powder particles, creating a thin solid layer of material. This process is repeated multiple times, fusing every new layer with the layer that is below until a solid 3-D object is complete.

The laser beam comes from an external laser source which is focused on a local spot of the powder bed by special laser optics. The scanning path is generated by scanning mirrors and galvanometers, which are moved by a controller connected to a CAD software.

Additionally, during the process, specific environmental conditions inside of the built chamber have to be achieved. Typically, nitrogen or argon is used to create an inert atmosphere to reduce the oxidation and degradation of the materials, especially for metals and alloys. Also, in plastic materials infrared heaters are usually used to warm up the powder just below the melting point or the glass transition temperature of the material. This is used to minimize the laser requirements of the process and achieve better final products (Gibson et al., 2015).

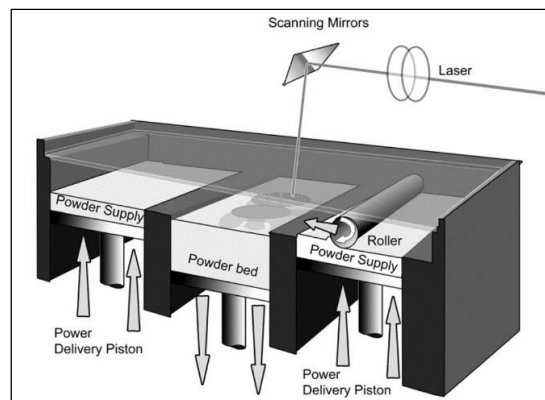


Figure 1-2: Selective laser sintering schematics of a two feed chamber machine (Hopkinson et al., 2005).

1.5.2. SLS Printing Parameters

Various printing parameters are involved in SLS, and the quality and mechanical properties of the final printed parts depend significantly on these parameters. The literature has covered extensively the effect of those parameters for different SLS materials. The main SLS printed parameters (Figure 1-3) are: laser power, scan speed, scan spacing (hatch distance), scan path, spot size, layer thickness, beam offset, and the scan count (number of times the laser beam traverses a scan vector per layer). Likewise, the following printed parameters also have significant influence: the sinter-scan (alternation of the x and y axes between layers), delay time, contour scan setting, skywriting, heat distribution, and thermal control of the powder bed (Goodridge et al., 2012).

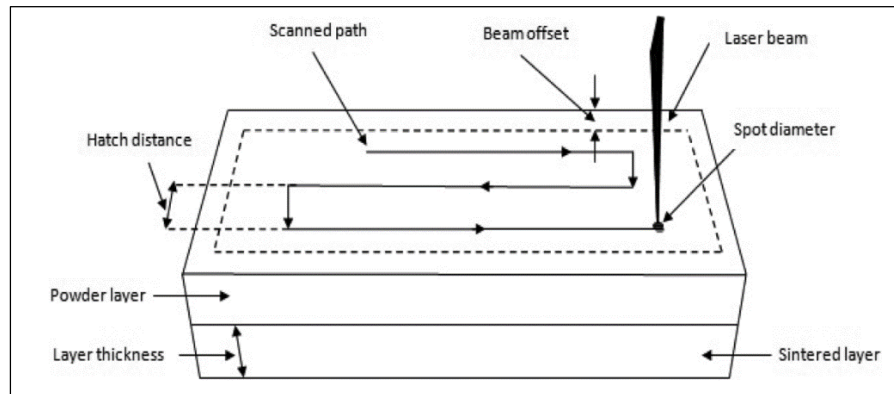


Figure 1-3: SLS printed parameters schematic (Negi et al., 2015).

The printed orientation also has been seen to be substantial in the mechanical properties of specimens due to the anisotropy behavior of the parts. Bassoli et al., 2012 fabricated specimens by SLS using an aluminum-filled polyamide and an alumina-polyamide composite material to investigate the mechanical properties and failure mechanisms, in comparison with unfilled PA. The result proves a relevant anisotropy between the bars printed horizontally and vertically, which depend on the efficacy of the strengthening mechanisms during the crack propagation, where the horizontal specimens showed a bigger area of ductile failure. Moreover, the elastic modulus is considerably higher for the filled materials than for the plain PA.

The energy density (ED) is a relevant parameter that is extensively used in SLS (Equation 2.1). The ED is function of the laser power (LP), laser speed (LS), and hatch distance (HD), which are the most influential and most common altered parameters in SLS.

$$ED = \frac{LP}{LS * HD} \quad (2.1)$$

Caulfield et al., 2007 studied the effect of energy density (ED) and orientation during the building on the density and mechanical properties such as yield strength, tensile strength, elongation, and Young's Modulus of laser sintered polyamide parts. They concluded that parts printed at high ED have better mechanical properties, and the orientation has significant effects on the tensile strength and elongation.

Jain et al., 2009 fabricated SLS polyamide specimens for different ranges of delay time, which depend on the orientation during building, to develop an algorithm to find the optimum value for tensile strength. The delay time (T_d) is the time difference between any two adjacent points on successive scanning lines on a layer, and can be calculated using Equation 2.2, where D is the distance travelled by the laser beam to scan the two consecutive points. Notice that the delay time depends on the scan path geometry, which can be varied by changing the scanning direction angles.

$$T_d = \frac{D}{LS} \quad (2.2)$$

They found that delay time influences the strength of parts significantly. The tensile strength improves significantly when the angle increases, reaching a optimum value at 60° , and then there is an abrupt drop between 60° and 90° (Figure 1-4).

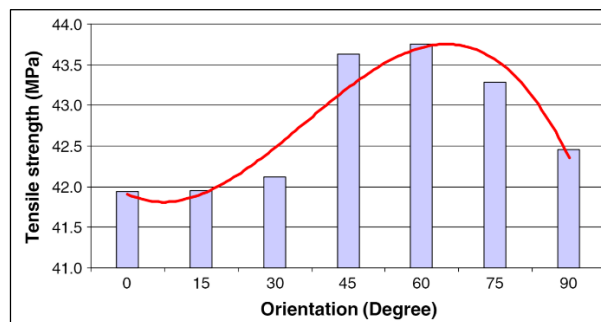


Figure 1-4: Tensile strength at various orientations based on delay time for EOS PA 2200 bars (Jain et al., 2009).

Degradation of polymers in air at high temperature is essentially oxidative in nature, and usually commercial machines use an inert atmosphere. However, so far our literature review has not shown studies about the effect of atmospheric oxygen during the fabrication process of SLS polyamide parts and its effect on SLS is not well known yet. In one investigation of injection molding, Nylon-6 and Nylon-66 yarns were exposed in air, nitrogen or vacuum to temperatures from 136 to 215°C for different periods of time. The ultimate tensile strength of the specimens was reduced by the exposure in the presence of oxygen (Valkot & Chiklis, 1965). A similar study investigated the influence of degradation behavior of polyamide 12 powder for SLS at different building chamber

temperatures and ambient conditions. The results showed that the process' material properties such as melt volume and viscosity were reduced by storing the powder under vacuum during the powder coating process (Wudy et al., 2014). A recent study on a thermoplastic elastomer material called PrimePart ST showed that the yellowish discoloration of the material depends on the concentration of atmospheric oxygen and the temperature. The material turns more yellowish at a high temperature (136 °C) and higher concentration of oxygen (atmospheric air), (Figure 1-5). However, the oxygen and temperature did not show a significant influence on the tensile strength and the elongation to fracture of the printed specimens (Kummert et al., 2017).

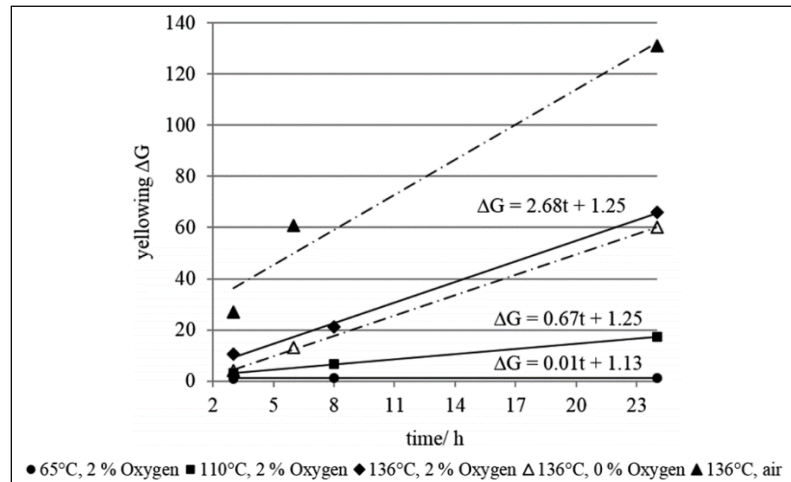


Figure 1-5: Yellowish discoloration of the material measured at different temperatures and oxygen levels (Kummert et al., 2017).

1.5.3. Consolidation Phenomena

Different consolidation mechanism occurs during the scanning process in SLS, and these depends on the nature of the material and the printing parameters used during the printing process. Kruth et al., 2007 reported the following consolidation mechanism:

- **Solid-state sintering:** is a consolidation process where the governing force is the minimization of total free energy of the powder particles. When particles reach elevated temperatures, $0.5 T_m$ (absolute melting temperature), the total surface area decreases, and thus surface energy decreases. Therefore, a diffusion between the

powder particles at solid stage creates necks between the adjacent particles, generating an agglomeration and voids between the particles, in order to reduce the total free energy of the powder (Figure 1-6). Then neck size increases and pore size decreases, reducing the total surface of the powder and consequently the sintering rate slows. To achieve very low porosity and dense parts longer sintering times, high sintering temperatures, or/and use of an external pressure are required. This can be done with hot isostatic pressing. Nevertheless, the diffusion rate also increases exponentially with higher temperatures and occurs rapidly when is close to the melting point. However, the solid-state sintering consolidation mechanism is the slowest, and usually is not fast enough to be the main mechanism in SLS. (Gibson et al., 2015). Ceramics powders are frequently governed by this consolidated mechanism.

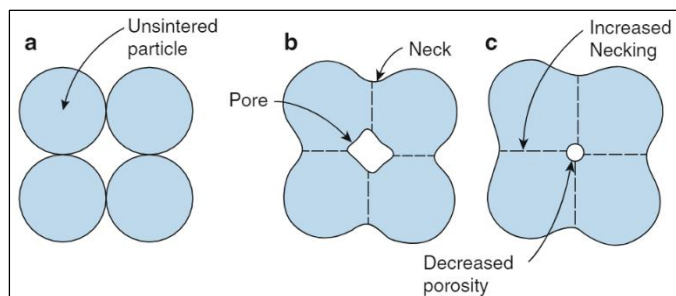


Figure 1-6: Sintering process. (a) Particles prior to sintering. (b) Particles start to agglomerate creating necks between them. (c) Neck size increase and pore size decrease during the sintering (Gibson et al., 2015).

- **Liquid phase sintering:** is a partial melting of the powder where one part of the powder material is melted while the rest remains solid. This consolidation mechanism happens when the melted material, also called the binder or additive, has a considerable lower melting point than the one that remains solid, also called the structural or base material. When the laser beam scanning raises the temperature of the powder, the binder material particles melt and spread between the solid particles, as it is driven by intense capillary forces. Then the molten material cools down which generates a matrix that adheres the solid particles

(Figure 1-7). The binder materials usually melt almost instantaneously, allowing much higher laser scan velocities. The binder and structural material can be combined in following ways: mixture of two-component powder (i.e. aluminum filled polyamide powder), composite powder particles where a micro structure contains both material, coated particles that have the binder material as a coating of the structural material, and indistinct mixture. In the case of this research a two-component powder is used (Figure 1-8).

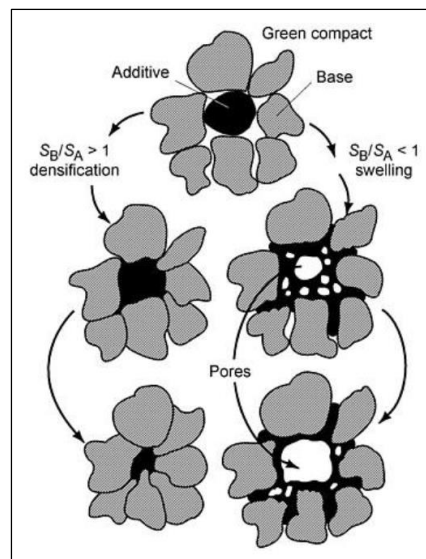


Figure 1-7: Sintering phase of composite powder material (Eisen et al., 1998).

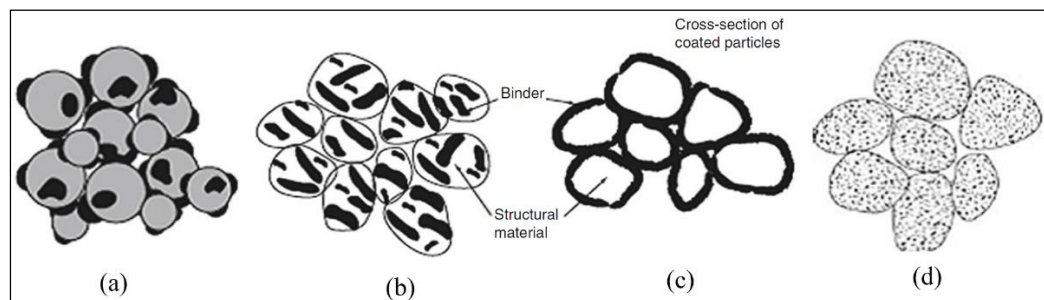


Figure 1-8. Different materials used in liquid phase sintering. (a) Mixture of two-component powder. (b) Composite powder particles. (c) Coated particles. (d) Indistinct mixture. The black regions are the binder material and the light regions are the structural material (Gibson et al., 2015).

- **Partial melting:** occurs when the powder particles only melts partially. This can happen with a single-phase material or a mixture of different powders but without similar binder and structural powder material. This consolidation mechanism can be classified in three ways. First, when the amount of energy from the laser beam is insufficient to melt the entire binder particle, the core remains solid. The molten material will adhere to the solid cores and the structural material. Second, when the powders have multiple phases or when a mixture of different powder particles are only partially molten. Third, when using a single material powder having a bi-modal distribution, where the small particles melt, while larger ones remains solid.
- **Full melting:** is a consolidation mechanism that completely melts the powder particles, and it is also known as Direct Metal Laser Sintering (DMLS). During the scanning process, the laser melts completely the powder particles and the melt pool exceed the layer thickness. The energy provided by the laser is sufficient to re-melt the previous layer, which creates a well-bonded part. DMLS is typically used in metal alloys and semi-crystalline polymers to print fully dense parts without post-process densification (Gibson, et al, 2015), (Kruth et al., 2007). Kruth et al., 2003 printed metallic parts with densities of 99.9% by using DMLS and reaching high energy densities in a small spot with the laser beam.
- **Chemical induced binding:** is not commonly used in commercial layer manufacturing, however is feasible for polymers, metals and ceramics. This consolidation mechanism binds the powder particles by a thermal activated chemical reaction. This exothermic reaction can be between two different types of powders or between atmospheric gases and the powder. Typically, the powders are pre-mixed and then heated up using low laser energies. Chemical induced binding is primary used in ceramic materials, and printed parts usually have low porosity; therefore, post-processes are needed, which increases the cost and time of fabrication. For this reason, the technologies that use this consolidation mechanism have not been commercialized successfully.

1.5.4. Energy Diffusion in SLS

During the laser scanning process, the laser beam melts the powder particles producing the meltpool. Several analytical solutions of the unsteady state heat equation have been used to model this behavior. The one-dimensional heat equation is defined as:

$$\frac{\partial T(z, t)}{\partial t} = \alpha \frac{\partial^2 T(z, t)}{\partial z^2} \quad (1.1)$$

where T is the temperature in function of the z -direction and time t and α is the thermal diffusivity of the material.

Franco et al., 2010 analyzed the SLS from an energy perspective, identifying the main energy terms during the scanning process at the melt pool (Figure 1-9). The energy provided by the laser beam in form of radiation interacts with the surface of the powder bed, where the radiation is reflected, transmitted and absorbed by the powder. The absorbed energy will be transferred by conduction, and the particles melt. Then, the molten mass cools down by heat transfer via radiation and convection to the environment. Furthermore, their study presents a different time dependent conduction model, neglecting convection and radiation. In this model, the laser beam modeled as a line heat source Q generates semi-cylindrical isotherms across the powder bed that can be expressed as:

$$T(r, t) - T_0 = \frac{Q}{4\pi kt} \exp\left(-\frac{r^2}{4\alpha t}\right) \quad (1.2)$$

where r is the radius, T_0 the initial temperature of the powder bed and k the thermal conductivity. Is important to notice that the temperature decrease exponentially over the radius; therefore, the energy does not penetrate deeply and only the particles close to the top surface will melt.

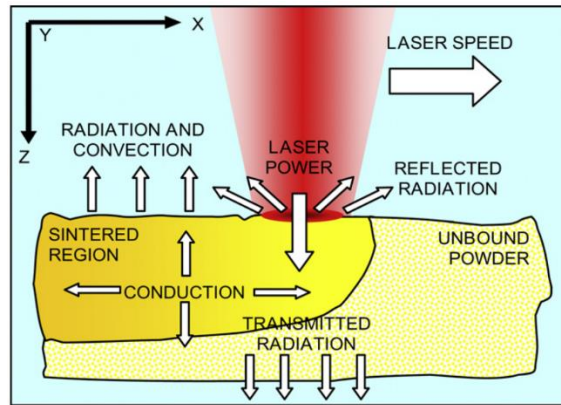


Figure 1-9: Main energy terms in the meltpool (Franco et al., 2010).

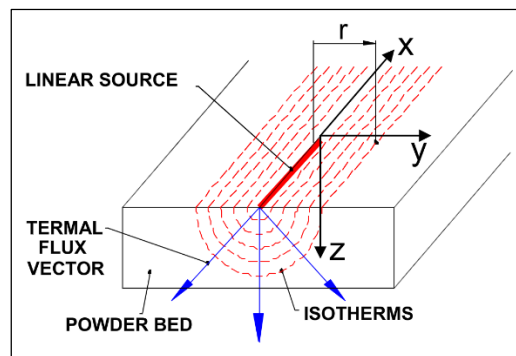


Figure 1-10: Isotherms caused by a linear source in the powder bed (Franco et al., 2010).

1.5.5. Design of Experiment

In order to quantify the effect of printed parameters in the mechanical properties of the specimen, an analysis of the variance (ANOVA) has to be performed for each response independently. The ANOVA test determines when the differences between the means are statistically significant, comparing the p-value with the significance level to assess the null hypothesis, which states that the means of the responses are all equal. Therefore, when the p-values are lower than 0.05 the factor can be considered significant for the response (Montgomery, 2012). The ANOVA assumptions – independence of cases, homoscedasticity, and normality of the residuals – have to be met to have a valid analysis. Main effects plots are used to examine the effect of different independent variables by plotting the means for each value of an independent variable. A steeper slope of the main

effects line has a greater effect than the independent has on the dependent variable. Interaction plots are used to visualize possible interactions, showing when one independent variable could affect another. Parallel lines indicate no interaction. A greater difference between the slope indicates a higher interaction between the factors.

Minitab 17 can calculate an optimized response maximizing the composite desirability of the responses. Individual and composite desirability are used to evaluate how well a combination of parameters satisfy a defined goal. Minitab 17 computes the individual desirability to evaluate every variable by itself using a utility transfer function, and the composite to evaluate how the settings optimize a set of responses overall, which is the weighted geometric mean of the individual desirability for the responses.

1.6. Preliminary Investigation

1.6.1. Material and methodology

A preliminary material characterization was performed to verify the chemistry of the powder particles and analyze the morphology of the EOS Alumide powder (EOS GmbH, 2012). A scanning electron microscopy (SEM) with an energy dispersive X-ray spectroscopy (EDS) was used to analyze a virgin powder sample. First, a virgin EOS Alumide sample powder was deposited on a small recipient. Second, an ultra-thin gold coating was applied on the sample to improve the imaging of the sample. Third, the sample was introduced into the SEM and two different types of particles were identified, images with different increments were taken. Finally, EDS analysis were applied on 4 different particles, two of each type, and the respective reports were compared.

1.6.2. Results and discussion

The EOS Alumide powder is a metallic grey, aluminum-filled polyamide 12 (PA-12) powder with particle sizes between 30 and 250 μm . The imaging revealed a two-component powder, where the aluminum is the structural material and the polyamide is the binder. Both types of particles have similar sizes but different shapes and roughness. The PA-12 particles show a spherical shape, rough surface, and are principally composed

of carbon, hydrogen, iridium, oxygen, and nitrogen (Figure 1-11). Considering that the chemical composition of the PA-12 is $[(\text{CH}_2)_{11}\text{C}(\text{O})\text{NH}]_n$, the high concentration of iridium was reviewed. This could be some additive to improve the properties from the supplier. The aluminum particles instead show an extended shape, are smoother than the PA-12 particles, and are composed of pure aluminum only (Figure 1-12).

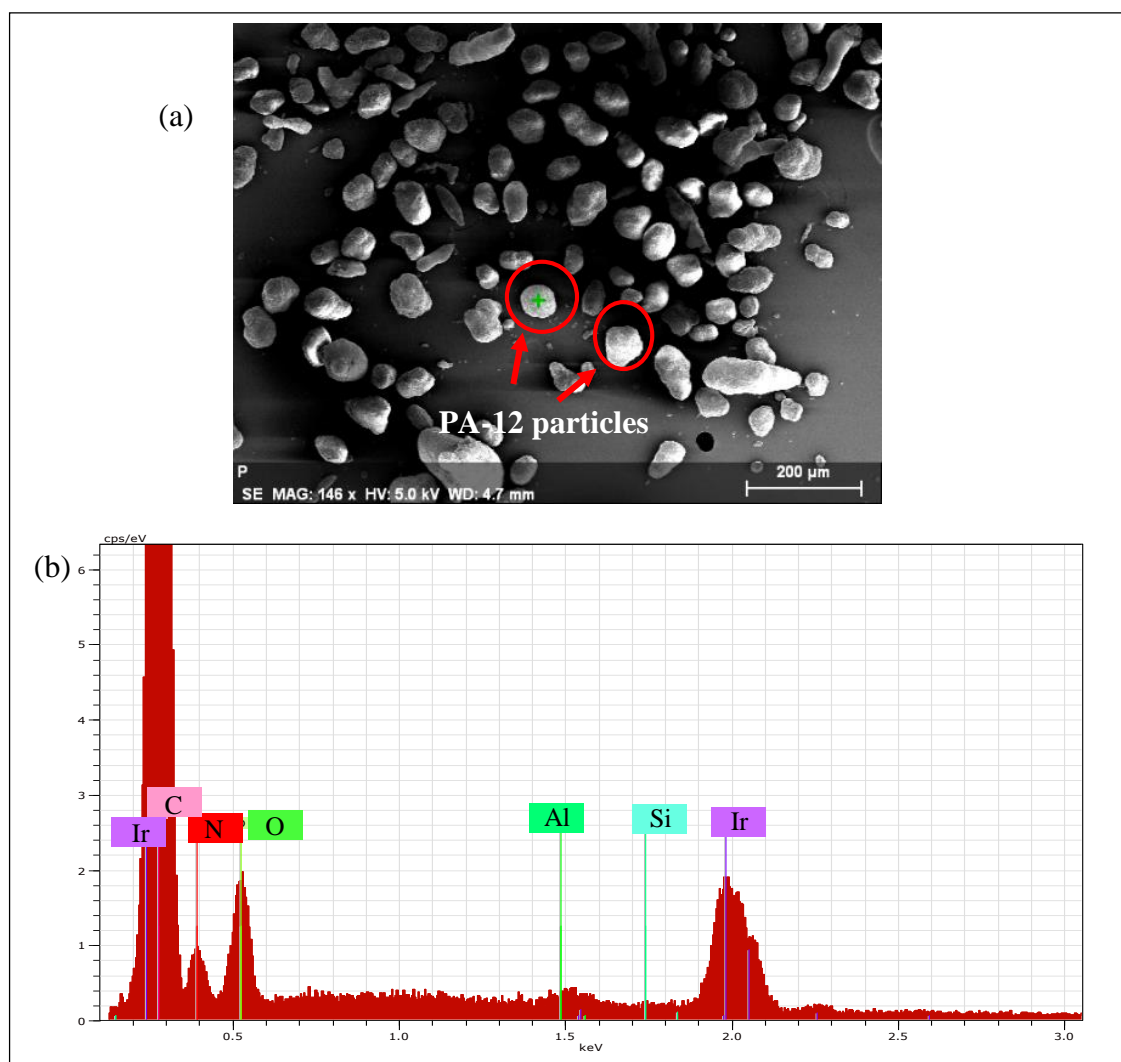


Figure 1-11: (a) Micrograph of the analyzed particle. (b) EDS analysis of a PA-12 particle.

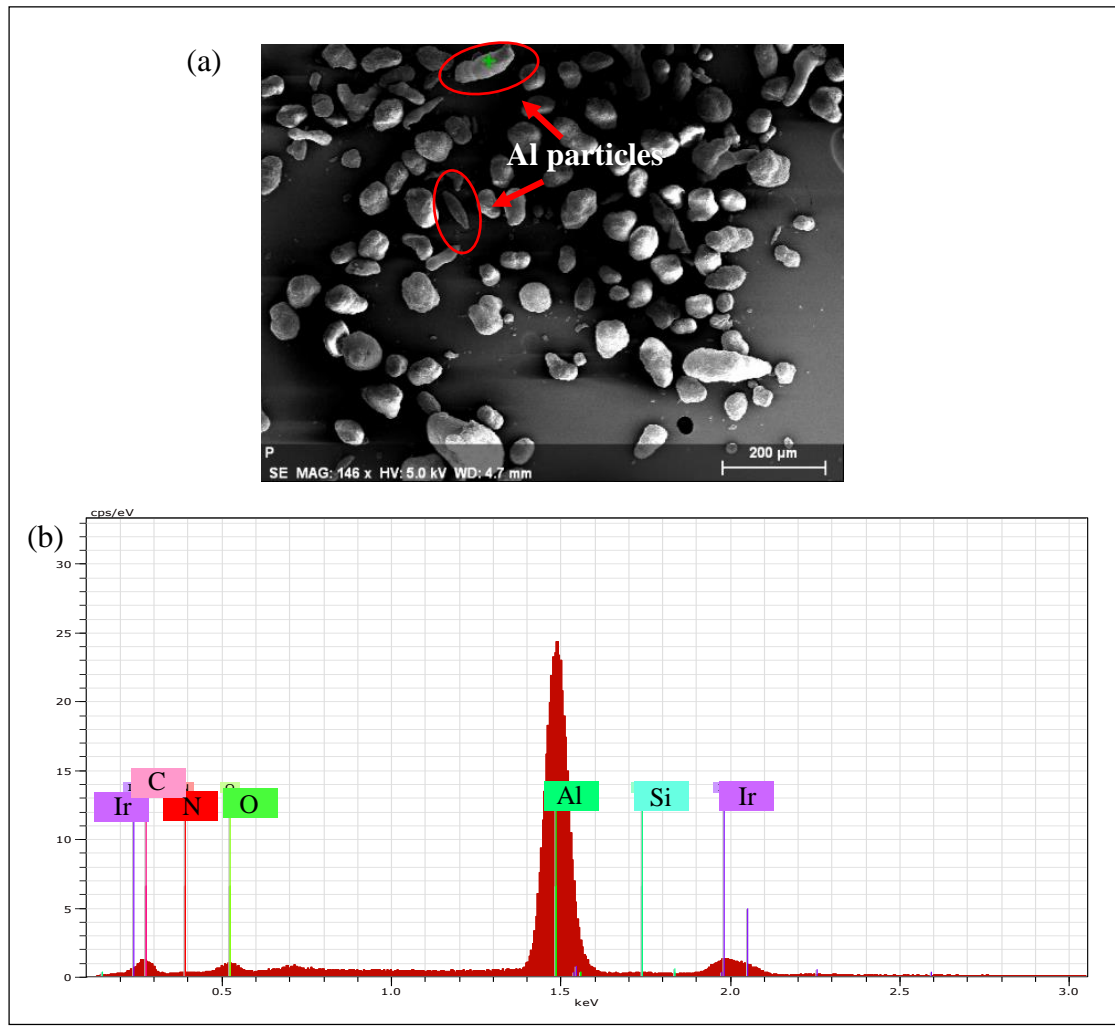


Figure 1-12: (a) Micrograph of the analyzed particle. (b) EDS analysis of an aluminum particle.

1.6.3. Conclusion

The EOS Alumide powder is two-component powder, with particles sizes between 30 and 250 μm. The aluminum (structural material) have a higher melting point than the polyamide (binder); therefore, during the scanning process the laser beam will melt the polyamide while the aluminum remains solid. The melted particles should spread between the solid particles by capillary force and a polyamide matrix might form. Additionally, the pores should not be bigger than 250 μm, because that is the maximum sizes of the particles. Bigger pores will suggest a degradation of the material.

2. MAIN ARTICLE: EFFECT OF SCANNING DIRECTION, ATMOSPHERIC OXYGEN AND LASER POWER ON MECHANICAL PROPERTIES OF SELECTIVE LASER SINTERING (SLS) OF ALUMINUM-FILLED POLYAMIDE MONOLAYERS

2.1. Abstract

In selective laser sintering (SLS) the quality and mechanical properties of the final printed parts depend strongly on the printing parameters. To better understand SLS on composite materials, this study focusses on the influence of scanning direction, atmospheric oxygen, and laser power on mechanical properties (ultimate tensile strength (UTS), elongation, density, and porosity), morphology, and joint mechanisms of laser-sintered aluminum-filled polyamide-12 (EOS Alumide) monolayer specimens.

The results show that a higher scanning angle and higher laser power significantly increase the UTS, elongation, and layer thickness. However, the oxygen level only has a small effect on the elongation to fracture. The oxygen level also shows small interactions with laser power or scanning angle. No changes in the morphology and internal structure in the specimens were observed using different sets of parameters. The morphology analysis revealed a composite structure formed by Al particles submerged in a molten polyamide matrix, where failure occurs at the polyamide. Two failure mechanisms were observed: a ductile failure that occurs when the particles are well-blended because the Al particles work effectively by obstructing crack propagations, and a fragile failure when the amount of Al particles is poor.

As a conclusion, oxidation and degradation of the material only have a small effect on the elongation to fracture and a small effect on the other properties when combined with laser power or scanning angle. Additionally, as expected, the scan path creates anisotropic parts, and the energy density has a significant effect on the mechanical properties.

2.2. Introduction

Selective laser sintering (SLS) is an additive manufacturing (AM) process that can build complex 3D-shaped parts. It consists of a laser beam that selectively sinters layer by layer

a bed of powdered material. SLS is extensively used in many different industries such as automobile, aeronautics, biomedical, and artistic (Bernard et al., 2009), (Negi et al., 2014), (Negi et al., 2015). Compared to others AM processes, SLS can use a wide range of materials like various types of polymers, metals and composites. It also does not usually require support structures, is a fully automatic process, is a speedy fabrication process, and has an easy post-processing treatment (Steen & Mazumder, 2010), (Negi et al., 2015). However, the SLS process is limited, because specimens fabricated by this technology have inferior tensile strength, tensile modulus, elongation, and the service life in comparison to the conventional polymer-processing techniques, such as injection molding, extrusion, thermoforming, and machining processes (Kruth et al., 2007).

The mechanical properties of polymers are lower compared to metals and ceramics; however, they can be improved by the inclusion of fillers, maintaining their lightweight and ductile nature. Therefore, composite materials are used in the polymer industry on specific applications, especially when stiff and robust parts are required. One of the advantages of SLS is the capability to process composite materials, like aluminum-reinforced polyamide, which have higher stiffness, thermal conductivity, and dimensional accuracy than unfilled polyamide (EOS GmbH, 2012). However, the mechanical properties of fabricated SLS polyamide parts not only depend on the used material, they are also influenced by several process parameters such as bed temperature, laser power, scan speed, scan spacing, layer thickness, delay time and many others (Goodridge et al., 2012).

Many research efforts have reported studies to improve the mechanical properties of parts produced by SLS. Mazzoli et al., 2007 characterized a new aluminum-filled polyamide powder developed for SLS application, and compared the new material to a commercial polyamide powder (DuraForm). They conclude that the material has a considerable high dimensional accuracy, strength and resistance to mechanical stress, and better finishing properties in comparison to the plain PA. Moreover, they show that the aluminum-filled polyamide is an opaque material to the X-rays and therefore can be used in biomedical applications (Mazzoli et al., 2007). Bazzoli et al., 2012 fabricated specimens by SLS using an aluminum-filled polyamide and an alumina-polyamide composite material to

investigate the mechanical properties and failure mechanisms, in comparison with unfilled PA. The result proves a relevant anisotropy between the bars printed horizontally and vertically, which depend on the efficacy of the strengthening mechanisms during the crack propagation, where the horizontal specimens showed a bigger area of ductile failure. Moreover, the elastic modulus is considerably higher for the filled materials than for the plain PA (Bassoli et al., 2012). Caulfield et al., 2007 studied the effect of energy density (ED) and orientation during the building on the density and mechanical properties such as yield strength, tensile strength, elongation, and Young's Modulus of laser sintered polyamide parts. They concluded that parts printed at high ED have better mechanical properties, and the orientation has significant effects on the tensile strength and elongation. The energy density (ED) that affects the part quality was calculated by equation 2.1, where LP is the laser power, LS the laser speed, and HD the hatch distance (Caulfield et al., 2007).

$$ED = \frac{LP}{LS * HD} \quad (2.1)$$

Jain et al., 2009 fabricated SLS polyamide specimens for different ranges of delay time, which depend on the orientation during building, to develop an algorithm to find the optimum for tensile strength. The delay time (T_d) is the time difference between any two adjacent points on successive scanning lines on a layer, and can be calculated using Equation 2.2, where D is the distance travelled by the laser beam to scan the two consecutive points. Notice that the delay time depends on the scan path geometry, which can be varied by changing the scanning direction angles (Jain et al., 2009).

$$T_d = \frac{D}{LS} \quad (2.2)$$

A significantly influence of the delay time on the strength was found. The tensile strength improves significantly when the angle increases, reaching a optimum value at 60° , and then there is an abrupt drop between 60° and 90° . The further drop on the tensile strength for between 60° and 90° (higher delay time), can happen due to insufficient power to sinter the powder particles. As well, Sabelle et al., 2018 obtained a similar behavior for the UTS

with respect to the scanning angle sintering Cu-Sn-Ni alloy metallic monolayers using different laser scanning speeds.

Degradation of polymers in air at high temperature is essentially oxidative in nature. In one investigation of injection molding, Nylon-6 and Nylon-66 yarns were exposed in air, nitrogen or vacuum to temperatures from 136 to 215°C for periods from 5 min. to 17.5 hr. The ultimate tensile strengths of the specimens were reduced in time by the exposure in air (Valkot & Chiklis, 1965). A similar study investigated the influence of degradation behavior of polyamide 12 powder for SLS at different building chamber temperatures and ambient conditions. The results showed that the process' material properties such as melt volume and viscosity were reduced by storing the powder under vacuum during the powder coating process (Wudy et al., 2014). A recent study on a thermoplastic elastomer material investigated the aging effect caused by the temperature histories and oxygen atmosphere on the color and mechanical properties of printed specimens of this material. The result revealed that the yellowish discoloration of the material depends on the temperature and the concentration of atmospheric oxygen. A higher discoloration was reached using an air atmosphere, instead of a nitrogen atmosphere (0% oxygen), and at higher temperatures. However, the mechanical properties – tensile strength and elongation – did not change with using different atmospheres (Kummert et al., 2017).

2.3. Experimental Procedure

To study the effects of the atmospheric oxygen, scanning direction and laser power on the mechanical properties and morphology of Alumide sintered monolayers, a chamber was built to vary the percent of atmospheric oxygen inside of it during the sintering process. To achieve successful and testable specimens, the printed parameters were adjusted, and the printed parameters windows were selected. Then, specimens were built combining the different parameters using one standard operating procedure, to ensure the repeatability and independence of the results, and different mechanical properties and morphology of the specimens were studied.

2.3.1. SLS Set-up and Material

The set-up used on the experiment (Figure 2-1) consisted of a chamber able to establish a controlled atmospheric pressure of about 0.2 to 6.0 bars. This chamber allows the percent of atmospheric oxygen inside of it to be changed by connecting it to a mechanical vacuum pump and a pressurized argon line. A Nd:YAG fiber glass laser YLR-300-AC-MM from IPG Photonics corporation was used to sinter the powder; the instrument has a maximum power of 300 W and a wavelength of 1.07 μm . The galvanometers of the laser were controlled by a DE controller series form General Scanning INC.

For the experiment, an aluminum-filled polyamide 12 powder material (Alumide) was used. The Alumide powder is a commercial material provided by EOS GmbH, which is characterized by its high stiffness, metallic grey appearance and good post-processing possibilities. In addition, laser sintered Alumide parts have excellent dimensional accuracy, well-balanced ratio of density stiffness, better thermal conductivity than parts fabricated from PA12, and good machinability. The surface of the parts can be refined by grinding, polishing and coating (EOS GmbH, 2012). Some properties of Alumide are listed on Table 2-1.

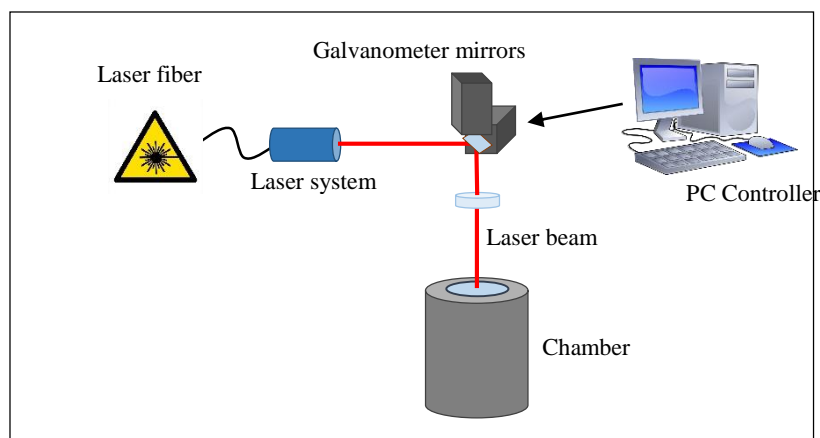


Figure 2-1: Experimental set-up schematic.



Figure 2-2: Chamber used to fabricate the specimens.

Table 2-1: Properties of Alumide powder (EOS GmbH, 2012).

Properties	Values
<i>Elastic modulus</i>	3.8 GPa
<i>Tensile strength</i>	48 MPa
<i>Melting temperature (20°C/min)</i>	176°C
<i>Density (laser sintered)</i>	1360 kg/m ³

2.3.2. Fabrication Procedure

A single layer of Alumide powder was sintered using a Nd:YAG fiber glass laser. The printed specimens had a size of 4.1 mm x 56 mm (Figure 2-7), where the thickness varies depending on different printing parameters. A design of experiment (DOE) was implemented to analyze the effect of different parameters. The angle of the scanning direction was varied on 3 levels (Figure 2-3), the oxygen was varied on 3 levels, and the power on 2 levels, obtaining a 3²x2 factorial design. Four replicates were printed for each combination of parameters (72 bars), three were used for tensile testing, and the other was used on the Micro CT porosity analysis. The DOE factors of interest were:

- Scanning direction angle (0°, 45°, and 60°)
- Laser Power (10 and 11 W)
- Oxygen inside the chamber (0.51%, 3.2%, and under atmospheric conditions)

The fixed printed parameters are shown on Table 2-2, and all the specimens were sintered at the same conditions, to ensure the repeatability of the experiment. It is important to highlight that the values used for the laser power, laser speed, and hatch distance are smaller than the usual values to laser sintered polyamide powders (Zarringalam et al., 2006). This set of parameters were selected after a calibration process on the machine. Considering the limitation of the galvanometers and its controller, different specimens were printed and tested using a laser power between 9 and 24 W; however, only the specimens at 10 and 11 W were printed successfully. At 9 W the power was not sufficient to fused the powder particles and at 12 W the degradation of the powder began to be observed. Additionally, that set of parameters were the best in order to fabricate thin monolayers to later be used on the tensile testing and others post-analysis.

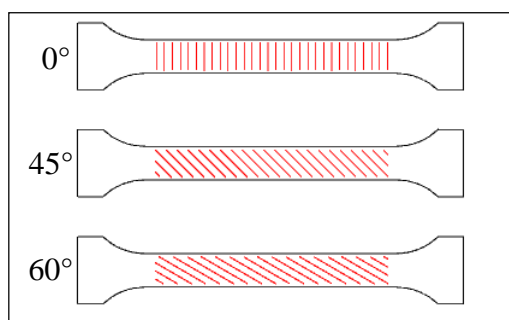


Figure 2-3: Scanning direction angles (0°, 45°, and 60°).

Table 2-2: Fixed printed parameters.

Fixed printed parameters	Values
<i>Laser speed</i>	78 mm/s
<i>Hatch distance</i>	0.05 mm
<i>Laser focused spot size</i>	0.24 mm
<i>Room temperature</i>	17 °C

To print the specimen, first, Alumide virgin powder was deposited in a receptacle 15 cm long, 4 cm wide, and 2 cm deep, forming a flat surface by spreading the top with a metallic spatula, where the laser will sinter the powder. Then the recipient was introduced inside of the chamber and the chamber was closed. The specimens were printed using two

different percentages of oxygen inside of the chamber. For the specimens printed under atmospheric conditions (21% of oxygen approx.), the chamber was maintained at atmospheric condition. On the other hand, for the specimens sintered at 0.51% and 3.2% oxygen (estimated values), first the pressure of the chamber was reduced using a mechanical vacuum pump down to 0.2 bar (absolute), and then the pressure was raised up to 6 bar (absolute) with pressurized argon, decreasing the percent of oxygen inside of the chamber. The percent of oxygen inside of the chamber (O_2) was estimated assuming the ideal gas law and using the Equation 2.3, where $O_{2\text{ atm}}$ is the percent of oxygen on the atmosphere (20.95 %), P_i is the initial pressure of the chamber (0.2 bar), P is the pressure at some instant, MW_{air} is the molecular mass of the air (29 g/mol), and MW_{Ar} is the molecular mass of the argon (39.9 g/mol).

$$O_2 = \frac{P_i MW_{\text{air}} O_{2\text{ atm}}}{P_i MW_{\text{air}} + (P - P_i) MW_{\text{Ar}}} \quad (2.3)$$

A positive pressure was used inside of the chamber, to ensure that the outside air was not filtering inside the chamber. Second, the software which controls the galvanometer and the laser were configured with the printing parameters. Then, the piece was sintered, and finally the pressure of the chamber was released carefully, and the specimen and the unfused powder were removed.

2.3.3. Characterization and Calibration

A caliper was used to measure the dimension of all the specimens. The height and width were measured after the fabrication of each specimen to corroborate that the size of the bar was correct. The thickness and the width of the specimens were calculated as the average of the measurement on two different points of the specimen after tensile testing and fracture.

Three specimen replicates were used for the tensile testing using a standard axial tensile tester (Instron), with a 4,900 N load cell and a crosshead speed of 1 mm/min to fracture, to obtain the ultimate tensile strength (UTS) and the elongation at fracture. The density of the bars sintered under atmospheric conditions was then measured applying the

Archimedes' method (Roman, et al., 1985). The bars were weighted under atmospheric conditions and then submerged in water. Equation 2.4 was used to calculate the densities of the specimens ρ , where ρ_{H_2O} is the density of the water (1000 kg/m³), W_{atm} the weight of the specimen on the atmosphere, and W_{H_2O} the weight in the water.

$$\rho = \frac{W_{atm} \rho_{H_2O}}{W_{atm} - W_{H_2O}} \quad (2.4)$$

The porosity of the specimens was measured from the non-tensile-tested replicates, using a 3D density and geometry phantom evaluation procedure and a MicroCT 80 (Scanco Medical). The specimens were submerged in a contrast of Dulbecco's phosphate buffered saline solution. The porosity of one specimen (printed angle 0°, laser power 10 W, and under atmospheric conditions) was estimated, to fix the parameters of the software used on the porosity evaluation. To calculate the porosity of the reference specimen, the system of equations 2.5 through 2.7 has to be solved, where ρ is the density of the specimen, ρ_{PA} the density of the PA-12 (1,010 kg/m³), ρ_{Al} the density of the aluminum (2,700 kg/m³), ρ_{air} the density of the air (1.225 kg/m³), x is the volumetric percent of the PA-12, y the volumetric percent of the aluminum, z the volumetric percent of the air of the specimen (porosity), and the weight percentage of aluminum in the material is 52% (Bassoli et al., 2012).

$$\rho = x \rho_{PA} + y \rho_{Al} + z \rho_{air} \quad (2.5)$$

$$x + y + z = 1 \quad (2.6)$$

$$\frac{y \rho_{Al}}{y \rho_{Al} + x \rho_{PA}} = 0.52 \quad (2.7)$$

A scanning electron microscopy (SEM) and an energy dispersive X-ray spectroscopy (EDS) were used to analyze a virgin Alumide powder sample and imaging some of the specimens. The upper and bottom surface, and the cross section on the fracture area after the tensile testing were analyzed.

2.3.4. Analysis of the Design of Experiment

In order to quantify the effect of printed parameters – laser power, scanning angle, and level of oxygen – in the mechanical properties – UTS, elongation, specimen thickness, and density – an analysis of the variance (ANOVA) was performed for each response independently, using the software Minitab 17. The results were analyzed by selecting order 3 model terms with a 95% confidence interval. The ANOVA assumptions – independence of cases, homoscedasticity, and normality of the residuals – were met for all the analysis. The assumptions were checked with different residuals plots (Montgomery, 2012) and using the Anderson-Darling test to verify the normality of the residuals. Main effects plots were used to examine the effect of different independent, and interaction plots were used to visualize possible interactions. An optimized response was calculated by the software Minitab 17 maximizing the composite desirability of the responses. Individual and composite desirability were used to evaluate how well a combination of parameters satisfy a defined goal.

2.4. Results and Discussion

2.4.1. Tensile Testing

A total of 54 test specimens were tensile tested. The ultimate tensile strength (UTS) and the elongation at fracture were measured for each bar. The tensile bars were printed with the same fixed parameters, and the scanning direction angles, laser power and the level of oxygen were modified factors of a $3^2 \times 2$ full factorial DOE. Three replicates were tested for each combination of parameters.

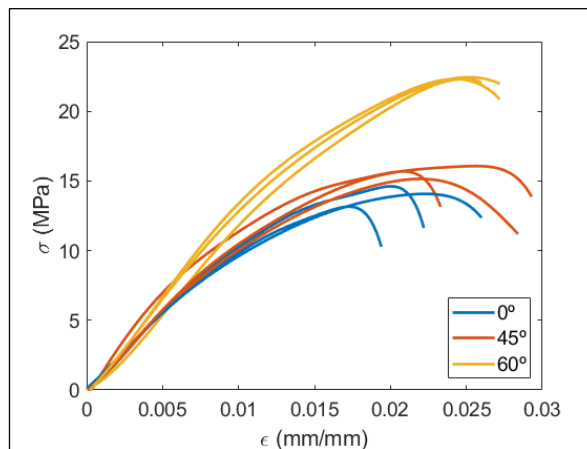


Figure 2-4: Stress(σ)-strain (ϵ) curves for specimens printed at 11 W and nominal atmospheric conditions at 0° , 45° and 60° .

The stress-strain curves obtained from the tensile testing have a similar shape for all the specimens. The slope of the curve decreases slowly reaching a maximum strength, then there is a decay in the strength specimens, and it fails catastrophically (elongation at fracture). Some examples of the stress-strain curves are shown in Figure 2-4. Additionally, similar behavior has been achieved on previous work using 3-D printed polylactic acid (PLA) (Kim et al., 2017), polyamide, and aluminum-filled polyamide specimens (Bassoli et al., 2012).

The results for the UTS and elongation are shown in Figure 2-5, and the ANOVA test for each response is presented on Table 2-3 and Table 2-4. The results for the UTS show a statistically significant effect for the scanning angle (p-value < 0.001) and the laser power (p-value = 0.002); however, the level of oxygen inside of the chamber has no effect on the UTS values.

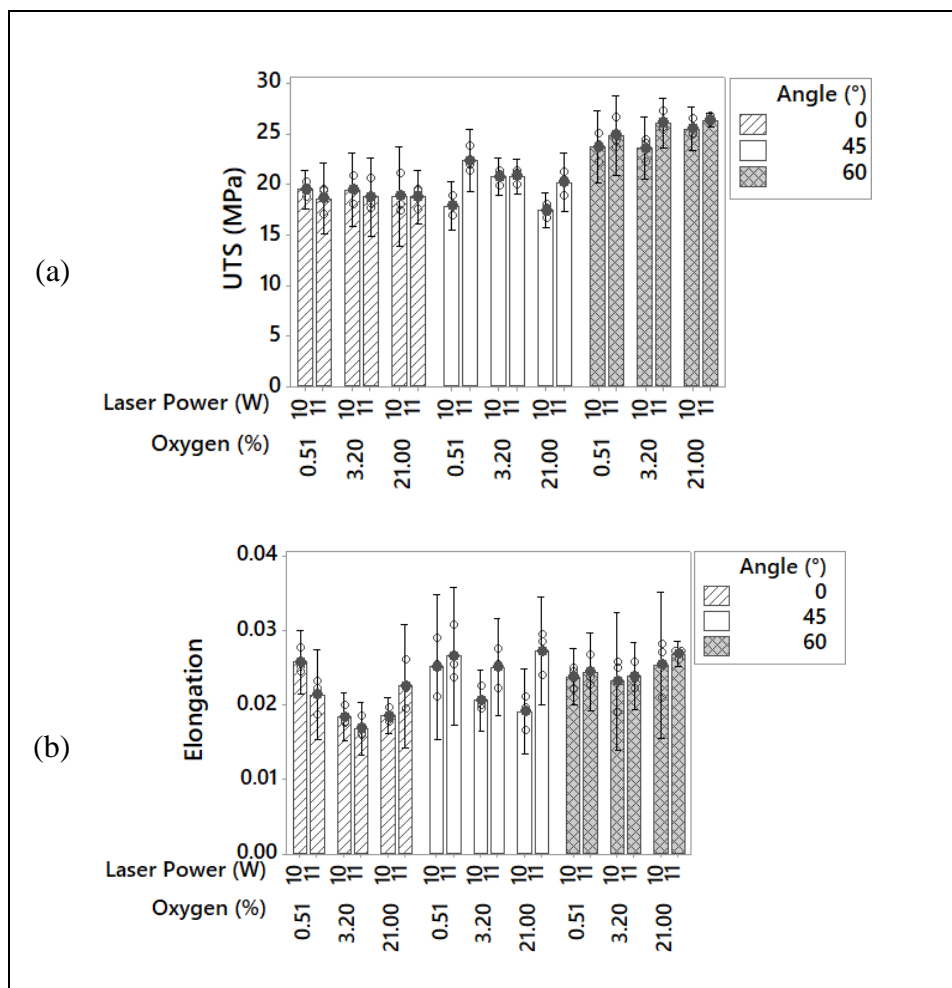


Figure 2-5: Ultimate tensile strength (a) and elongation (b) versus scanning direction angle.

Figure 2-6a shows how increasing the scanning angle causes a considerable increase on the UTS, where the maximum value is reached using an angle of 60°. An increase of 4.6% and 31.8% on the UTS means it is achieved using 45° and 60° angles respectively, with respect to the samples printed at 0°. In the same way, an increase of the laser power also increased the results for the UTS by 6.0%. The interaction between the angle and the laser power is the most significant (p -value = 0.004) but only between 0° and 45°. The interaction between the angle and oxygen is also statistically significant (p -value = 0.039), where the highest value of UTS is reached at nominal atmospheric conditions and 11 W.

The rest of the interactions between the factors do not show significant effects on the response (Figure 2-6b).

For the elongation all the factors show a statistically significant effect. The scanning angle is the most influential, with a p-value < 0.001 . Figure 2-7 shows a big increase of the mean from 0° to 45° and then a smaller increase from 45° to 60° . Then, the oxygen level has a significant effect on the elongation of the specimen (p-value=0.002). The elongation decreases by 13.0 % between 0° and 45° but then only by 5.0 % for 60° with respect to samples printed at 0° . Elongation is also proportional to the laser power, where the average elongation increased by 7.4% from 10 to 11 W. Similar behavior can be noticed in the plots in Figure 2-5, where the maximum values are reached using a laser power of 11 W with an angle of 60° . All interactions between two factors show an influence of the elongation, where the most important is the combination of laser power and angle, and the less significant is the combination of angle and oxygen level.

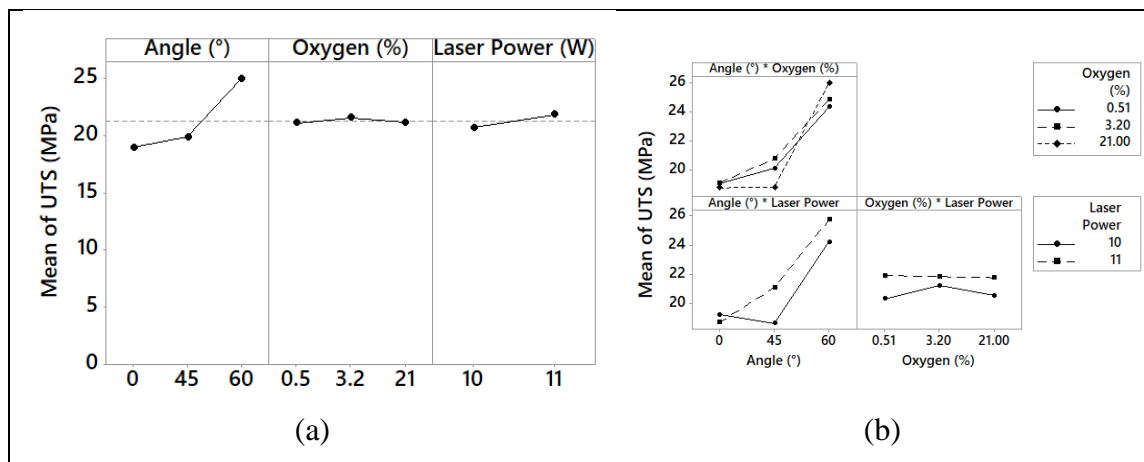


Figure 2-6: (a) Main effect plots, and (b) interactions plots for UTS.

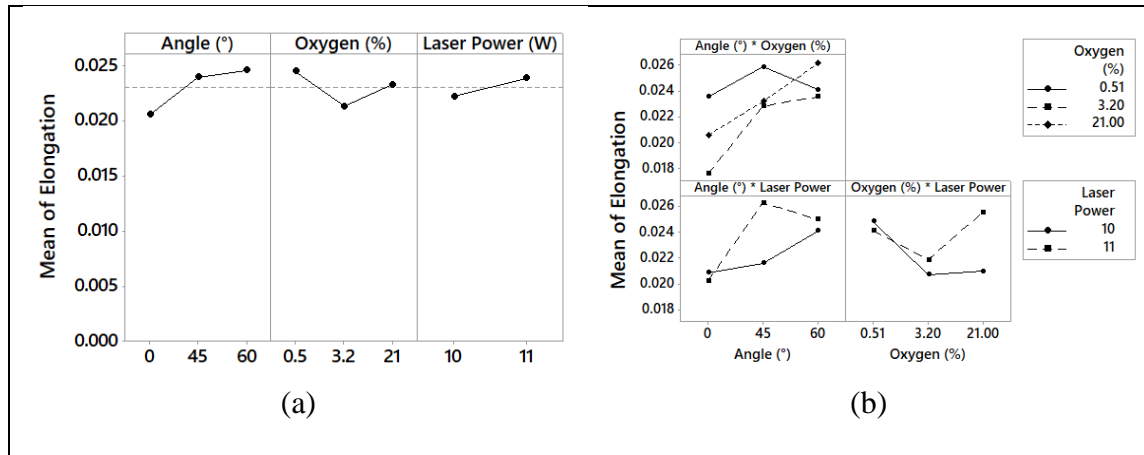


Figure 2-7: (a) Main effect plots, and (b) interactions plots for elongation.

Table 2-3: Ultimate tensile strength ANOVA test results.

<i>Model terms</i>	Degree of freedom	Adjusted sum of squares	Adjusted mean square	F-Value	P-Value	
<i>Model</i>	13	442.659	34.051	20.21	< 0.001	
<i>Linear</i>	5	400.65	80.13	47.55	< 0.001	
<i>Angle</i>	2	381.109	190.555	113.08	< 0.001	significant
<i>Oxygen</i>	2	1.953	0.977	0.58	0.565	
<i>Laser Power</i>	1	17.588	17.588	10.44	0.002	significant
<i>2-Way Interactions</i>	8	42.008	5.251	3.12	0.008	
<i>Angle * Oxygen</i>	4	18.779	4.695	2.79	0.039	significant
<i>Angle * Laser Power</i>	2	21.109	10.555	6.26	0.004	significant
<i>Oxygen * Laser Power</i>	2	2.12	1.06	0.63	0.538	
<i>Error</i>	40	67.404	1.685			
<i>Total</i>	53	510.063				
S	R ²	R ² (adjusted)	R ² (predicted)			
1.29811	86.79%	82.49%	75.92%			

Table 2-4: Elongation at fracture ANOVA test results.

<i>Model terms</i>	Degree of freedom	Adjusted sum of squares	Adjusted mean square	F-Value	P-Value	
<i>Model</i>	13	0.000497	0.000038	5.91	< 0.001	
<i>Linear</i>	5	0.000296	0.000059	9.16	< 0.001	
<i>Angle</i>	2	0.000167	0.000083	12.87	< 0.001	significant
<i>Oxygen</i>	2	0.000093	0.000046	7.16	0.002	significant
<i>Laser Power</i>	1	0.000037	0.000037	5.71	0.022	significant
<i>2-Way Interactions</i>	8	0.000201	0.000025	3.88	0.002	
<i>Angle * Oxygen</i>	4	0.000068	0.000017	2.64	0.048	significant
<i>Angle * Laser Power</i>	2	0.000068	0.000034	5.22	0.01	significant
<i>Oxygen * Laser Power</i>	2	0.000065	0.000032	5.02	0.011	significant
<i>Error</i>	40	0.000259	0.000006			
<i>Total</i>	53	0.000756				
S	R ²	R ² (adjusted)	R ² (predicted)			
0.0025432	65.76%	54.63%	37.60%			

2.4.2. Delay Time

The delay time is defined as the time difference between any two adjacent points on successive scanning lines on a layer and depends on the scan path geometry, which can be varied by changing the scanning direction angles. Jain et al., 2009 found that delay time influences the strength of PA-12 laser sintered bars significantly. The tensile strength improves significantly when the angle increases, reaching a optimum value at 60°. This can be attributed to thermal degradation of polyamide due to the long exposure to the laser beam. The experimental results of the present study in Figure 2-8 show a similar behavior for Alumide monolayers bars, where the maximum UTS is reached at 60°. It can be seen in Figure 2-5a that at low delay time (low angle) the part strength is smaller. Moreover, the literature has reported for different materials (Kim et al., 2017), (Sabelle et al., 2018) that the anisotropy of the specimens has an important effect on the strength and elongation of the printed parts due to the scanning processes. The strength and elongation are more likely to be lower when scanning and loading directions are perpendicular to each other.

The energy density (ED) is 2.56 and 2.82 J/mm² for the bars printed at 10 and 11 W, respectively. The values of tensile strength and elongation are related to the ED of each specimen, where the highest mechanical properties are measured from the specimens with the highest ED. When the laser power increases, ED also increases, and the melt starts to flow and filling the gaps between the aluminum particles, producing a stronger cohesion between the powder particles; therefore, the mechanical properties improve (Gibson et al., 2015). Therefore, as you get a larger melt pool due to higher ED, then the oxygen plays a role in degrading the polymer, so one should see two competing forces: polymer degradation vs more molten mass to resist tensile forces. Eventually the higher amount of degradation could be offset by a larger mass of molten polymer.

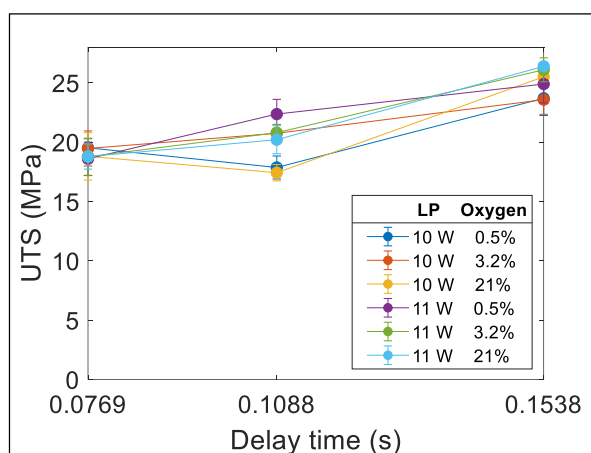


Figure 2-8: UTS results versus delay time.

2.4.3. Specimen Thickness

The thickness of each specimen was measured using a caliper three times in three different parts of the bars, and the mean values were used for the analysis, additionally, three replicates were used for each group of bars. Figure 2-9 and Figure 2-10a show how the thickness does not change significantly from 0° through 45°, however, it increases using a scanning angle of 60°. Furthermore, from the ANOVA test (Table 2-5) it can be seen that the angle has a statistically significant effect on the thickness, due to the higher values at 60°. As was expected, thicker bars were printed with the higher laser power setting. A

higher laser power will provide a higher amount of energy to melt and sinter the powder particles, therefore, the melting pool will be bigger, cohering deeper and adjacent particles and producing a thicker layer. Figure 2-10 shows an increase on the means of 8.9 % from 10 to 11 W and the ANOVA test confirms a significant effect for the laser power. Sabelle et al., 2018 obtained similar results for Cu-Sn-Ni alloy metallic sintered monolayers, where thicker bars were fabricated by higher laser power. The statistical analysis suggests that the oxygen level has a significant effect on the specimen thickness; however, the calculated p-value is 0.043. Bearing in mind that a factor is considered significant when the p-value is lower than 0.05 and observing the results in Figure 2-9 and Figure 2-10, the oxygen level has no significant effect in the thickness of the bars.

The interaction between the angle and laser power has the most significant effect on the thickness (p-value = 0.027), where the thinner bars are fabricated by 45° at with 21% of oxygen, and the thicker specimens at 60° with both atmospheres (Figure 2-10). The scanning angle – oxygen interaction has a significant effect as well (p-value = 0.031); however, the bars printed by 11 W do not vary in thickness with the changes in the oxygen level. The interaction between the level of oxygen and laser power can be considered insignificant since the p-value is only 0.043 and the interaction plots show no large difference between the slopes.

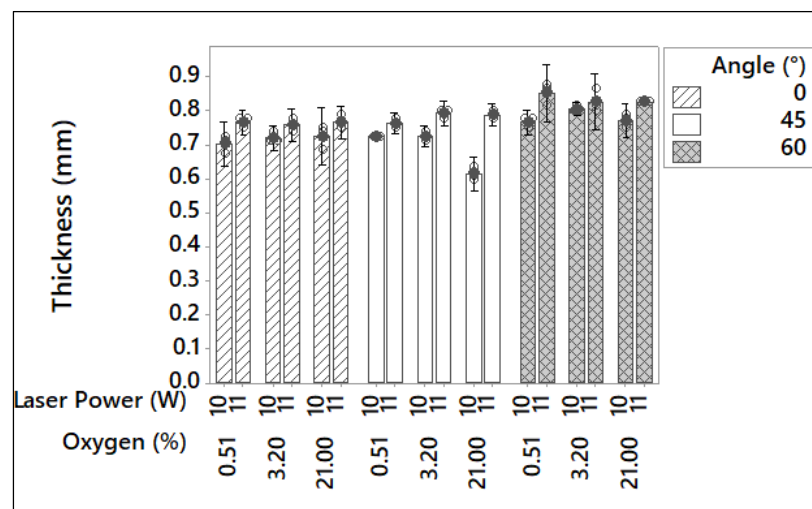


Figure 2-9: Specimen thickness versus scanning direction angle.

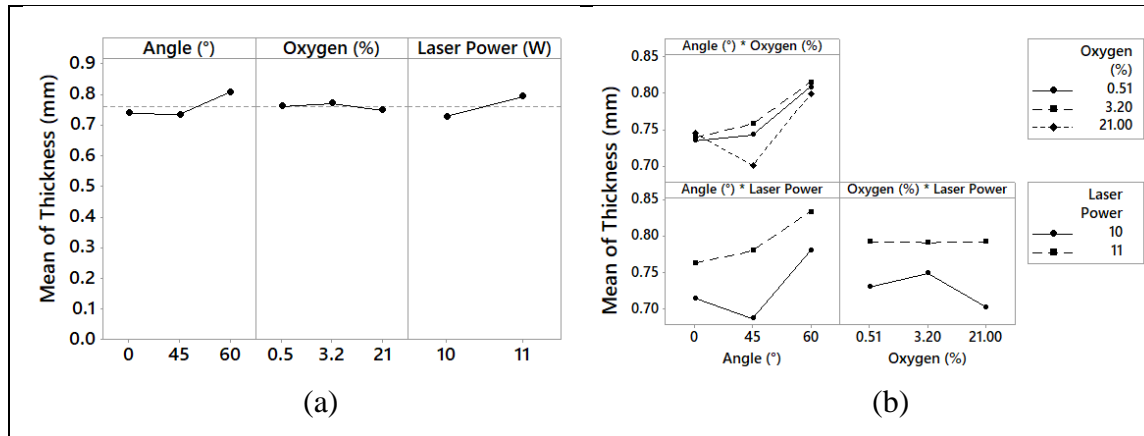


Figure 2-10: (a) Main effect plots, and (b) interactions plots for specimen thickness.

Table 2-5: Specimen thickness ANOVA test results.

<i>Model terms</i>	Degree of freedom	Adjusted sum of squares	Adjusted mean square	F-Value	P-Value	
<i>Model</i>	13	0.139361	0.01072	15.57	< 0.001	
<i>Linear</i>	5	0.121589	0.024318	35.31	< 0.001	
<i>Angle</i>	2	0.060024	0.030012	43.58	< 0.001	significant
<i>Oxygen</i>	2	0.004683	0.002342	3.4	0.043	
<i>Laser Power</i>	1	0.056882	0.056882	82.6	< 0.001	significant
<i>2-Way Interactions</i>	8	0.017772	0.002221	3.23	0.006	
<i>Angle * Oxygen</i>	4	0.007091	0.001773	2.57	0.052	
<i>Angle * Laser Power</i>	2	0.005448	0.002724	3.96	0.027	significant
<i>Oxygen * Laser Power</i>	2	0.005233	0.002616	3.8	0.031	significant
<i>Error</i>	40	0.027545	0.000689			
<i>Total</i>	53	0.166905				
S	R ²	R ² (adjusted)	R ² (predicted)			
0.0262415	83.50%	78.13%	69.92%			

2.5.3. Density and Porosity

The apparent density of the 54 bars was measured using the Archimedes' method and an ANOVA test was performed on the results (Table 2-6). No influences of the variables and their interactions were found for the density. This means that the used range of laser power was not big enough to cause any effect on the density, and the level of oxygen and scanning angle have no influence on the response. Previous research has proven that the

laser power has a critical role on the apparent density, where higher values of laser power (higher ED) produce denser parts, since more energy is provided to merge the powder particles. However, an optimum point exists because an excess of energy will melt, vaporize, and degrade the particle powder, making bubbles inside of the bar (Caulfield et al., 2007), (Kruth et al., 2007), (Sabelle et al., 2018). Additionally, a Micro CT was used to measure the porosity of one bar of each group. As was expected, Figure 2-11 confirms that the results for the density and porosity are correlated. Larger pores or a higher concentration of pores will generate a higher porosity. Consequently, more void space will be contained inside the specimens, reducing the density of the part. Furthermore, the plots verified that the factors do not have a significant effect on the density and porosity.

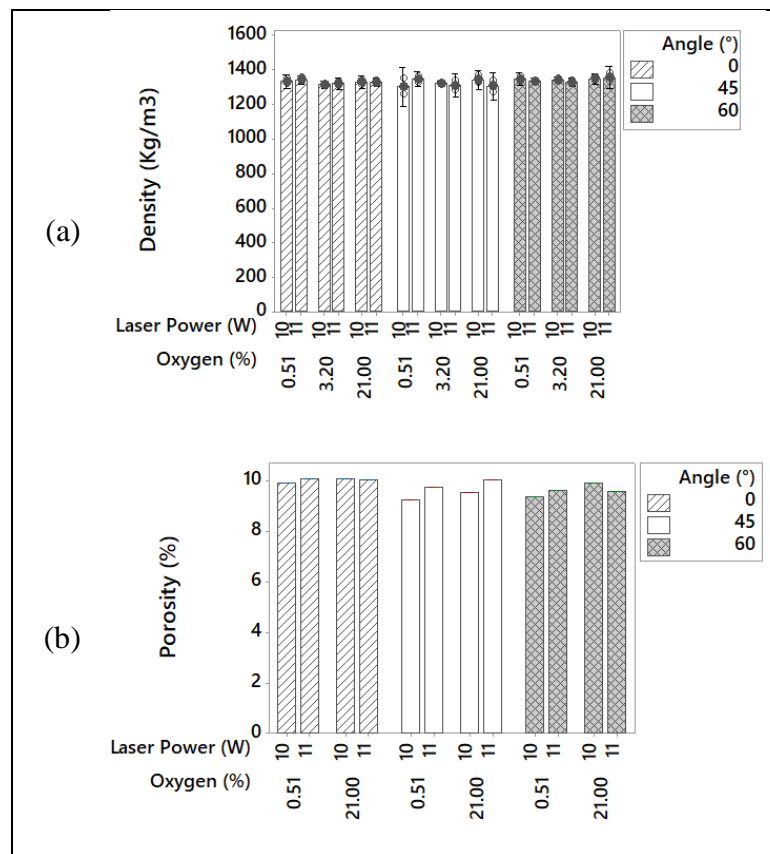


Figure 2-11: Density (a) and porosity (b) versus scanning angle plots.

Table 2-6: Density ANOVA test results.

<i>Model terms</i>	Degree of freedom	Adjusted sum of squares	Adjusted mean square	F-Value	P-Value
<i>Model</i>	13	8081.3	621.64	1.44	0.186
<i>Linear</i>	5	5672.1	1134.43	2.62	0.039
<i>Angle</i>	2	4032.3	2016.15	4.66	0.015
<i>Oxygen</i>	2	1627	813.52	1.88	0.166
<i>Laser Power</i>	1	12.8	12.8	0.03	0.864
<i>2-Way Interactions</i>	8	2409.2	301.15	0.7	0.693
<i>Angle * Oxygen</i>	4	782.6	195.65	0.45	0.77
<i>Angle * Laser Power</i>	2	234.9	117.45	0.27	0.764
<i>Oxygen * Laser Power</i>	2	1391.7	695.86	1.61	0.213
<i>Error</i>	40	17321.6	433.04		
<i>Total</i>	53	25402.9			
S	R ²	R ² (adjusted)	R ² (predicted)		
20.8096	31.81%	9.65%	0.00%		

2.5.4. Optimized Response

From the results obtained from the ANOVA tests and using the commercial software Minitab, an optimized response was predicted. The best set of parameters of this study were calculated in order to achieve the best mechanical properties within the experimental range, maximizing the responses of the UTS, elongation, and density. In order to calculate the optimum parameters, a regression equation was calculated for each response. Then, based on those equations an optimum parameter was found based on predicted values computed from those equations. The specimen thickness was excluded from the analysis because it is not a mechanical property, but rather an effect from the parameters used. It can be clearly observed from the optimization plot (Figure 2-12) that the best properties are reached for all the responses printing with a scanning angle of 60°, laser power of 11 W, and air (Table 2-7). Furthermore, the obtained optimum parameters match the results discussed in the previous sections. The optimized results were the same of an experimental point; however, this is just coincidence because the analysis is based on a continuous function. This analysis cannot extrapolate values over the experimental range; therefore, a better set of parameters can be found using parameters out of this range. Table 2-8

compares the predicted values from the analysis with the obtained experiment results. The results are almost identical, which verifies the analysis. Nevertheless, both results are considerably lower in comparison with the values provided by powder supplier on the EOS Alumide Material Data Sheet (MDS) (EOS GmbH, 2012). This can be explained by the fact that the EOS MDS values are given for 3-D parts (multilayers). Since monolayers bars were printed for this research, the printed parameters were modified in order to achieve successful parts; therefore, the mechanical properties are lower.

Table 2-7: Optimum parameters of the experiment.

Parameters	Angle	Oxygen	Laser Power
Values	60°	21%	11 W

Table 2-8: Predicted optimized response compared with experimental results and EOS MDS values (EOS GmbH, 2012).

Response	Prediction	Results	EOS MDS
UTS (MPa)	26.74 ± 0.66	26.38 ± 0.03	48
Elongation (%)	2.802 ± 0.129	2.686 ± 0.068	4
Density (kg/m^3)	1341 ± 11	1353 ± 25	1360

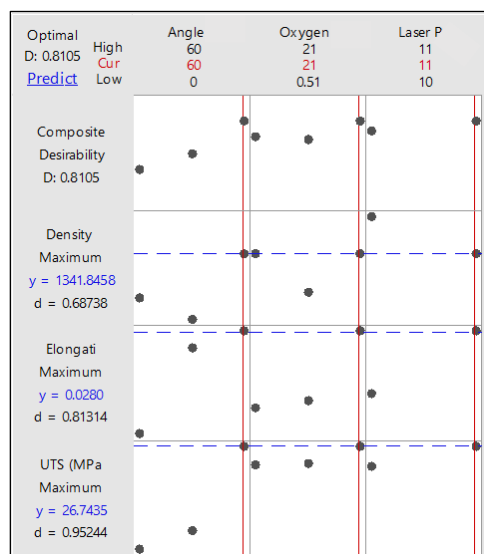


Figure 2-12: Optimization plot maximizing the UTS, elongation, and density responses.

2.5.5. Morphology

The EOS Alumide powder is a mix between PA-12 and aluminum particles, where the particle size is between 30 and 250 μm (Figure 2-13). The PA-12 particles have a spherical shape, are rougher than the aluminum particles, and are principally composed of carbon, iridium, oxygen, and nitrogen. The aluminum particles instead show an extended shape, are smoother, and are composed of pure aluminum only.

A scanning electron microscopy (SEM) was used to analyze both the cross section at the fractured area after the tensile testing and the upper and bottom surfaces of the specimens. After the analysis, no differences were found in the morphology between the specimens, and all of them show similar characteristics.

As composite material, two distinct areas can be differentiated in the specimens as shown in Figure 2-14, where filled reinforcement Al particles are submerged in a polyamide matrix. The melting temperature for the PA-12 is 176°C (EOS GmbH, 2012) and for Al is closed to 660°C. This difference in the melting point produces the composite material. The laser beam increases the temperature of the powder enough to melt the polyamide and heat the Al particles, creating a meltpool. Then the melted polyamide starts to flow filling the gaps between the Al particles and surrounding them, generating a strong and dense part. Similar joining mechanisms have been seen for laser-sintered glass-filled polyamide bars (Negi et al., 2014), (Negi et al., 2015).

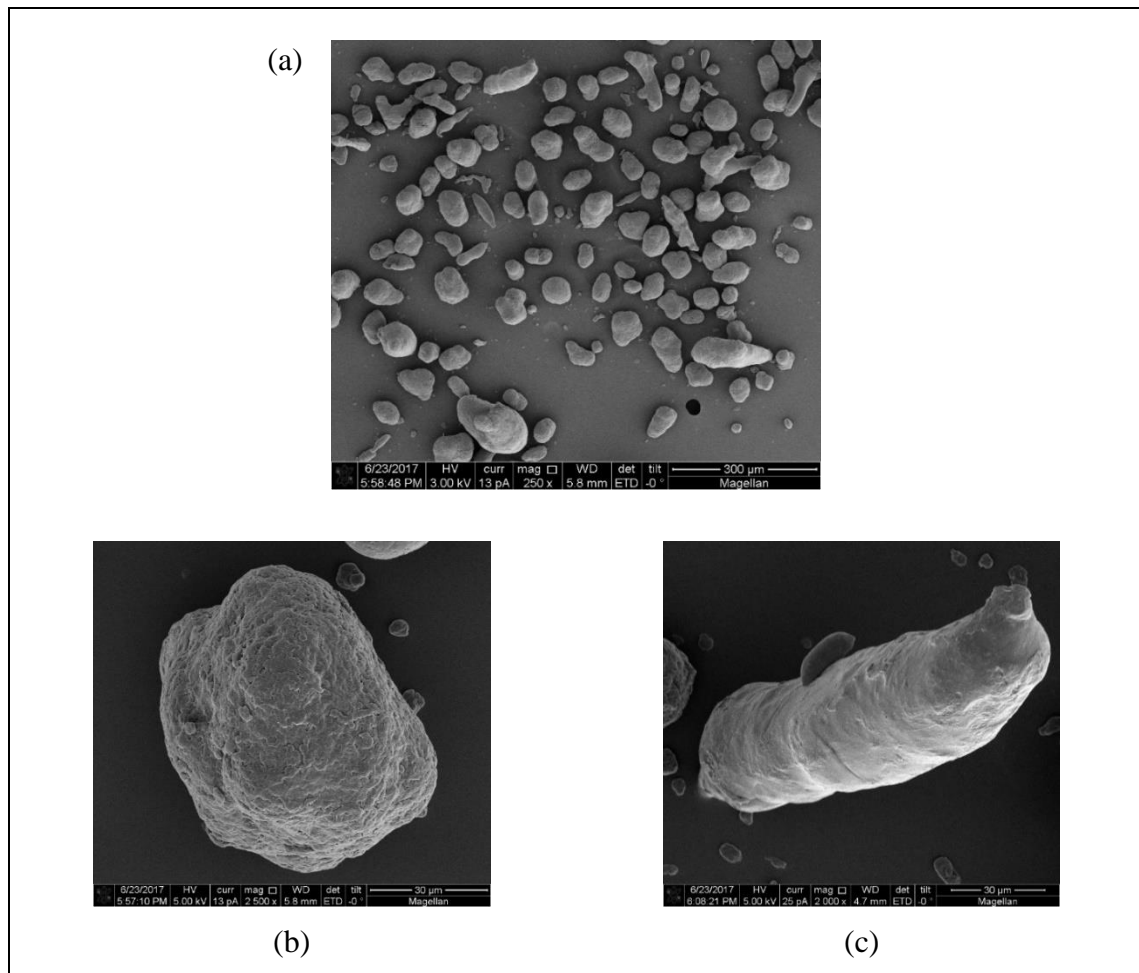


Figure 2-13: SEM images of Alumide powder. (a) Virgin powder sample (250x).
 (b) PA-12 particle (2500x). (c) Aluminum particle (2000x).

Two failure mechanisms were clearly identified in different regions of the specimens, due to signs of strain of the polyamide. First, a ductile failure can be observed in Figure 2-14a through Figure 2-14c. The ductile failure occurs in large areas at the middle of the specimens, where the Al particles emerged from a deformed, stretched and torn polyamide matrix. This phenomenon can be justified considering the stiffness of the different materials and the distribution of the particles. On one hand, the aluminum has a considerably higher yield point and Young's modulus than the polyamide; therefore, failure occurs only in the polyamide matrix. On the other hand, in the well-blended areas the distribution of the Al particles is effective by obstructing crack propagations, which

leads to the polyamide yields and causes a ductile failure. Second, fragile failure zones were identified at different areas of the specimens. Fragile failure zones occur where there is an absence or low amount of Al particles in an area of the specimens because the cracks can propagate easily without obstruction. Fragile failure zones were usually found at the top since Al is denser than polyamide; therefore, when the polyamide particles melt the Al particles sink and form a top layer of polyamide. This phenomenon can be seen clearly in Figure 2-14b, where all Al particles are covered by a layer of polyamide. Moreover, it has been noticed in previous research (Kruth et al., 2007) that aluminum-filled polyamide powder often shows coagulation, since the mixing process is not always useful due to the difference in size and density of the particles. Figure 2-14d shows an amplification of the fragile failure zone in Figure 2-14a, where it can be seen that no Al particles are present in that zone due to the coagulation of the polyamide particles. Since nothing stops crack propagation across the polyamide matrix, a fragile failure occurs on that zone. Bassoli et al., 2012 observed the same failure mechanisms on laser-sintered aluminum-filled polyamide multilayer bars.

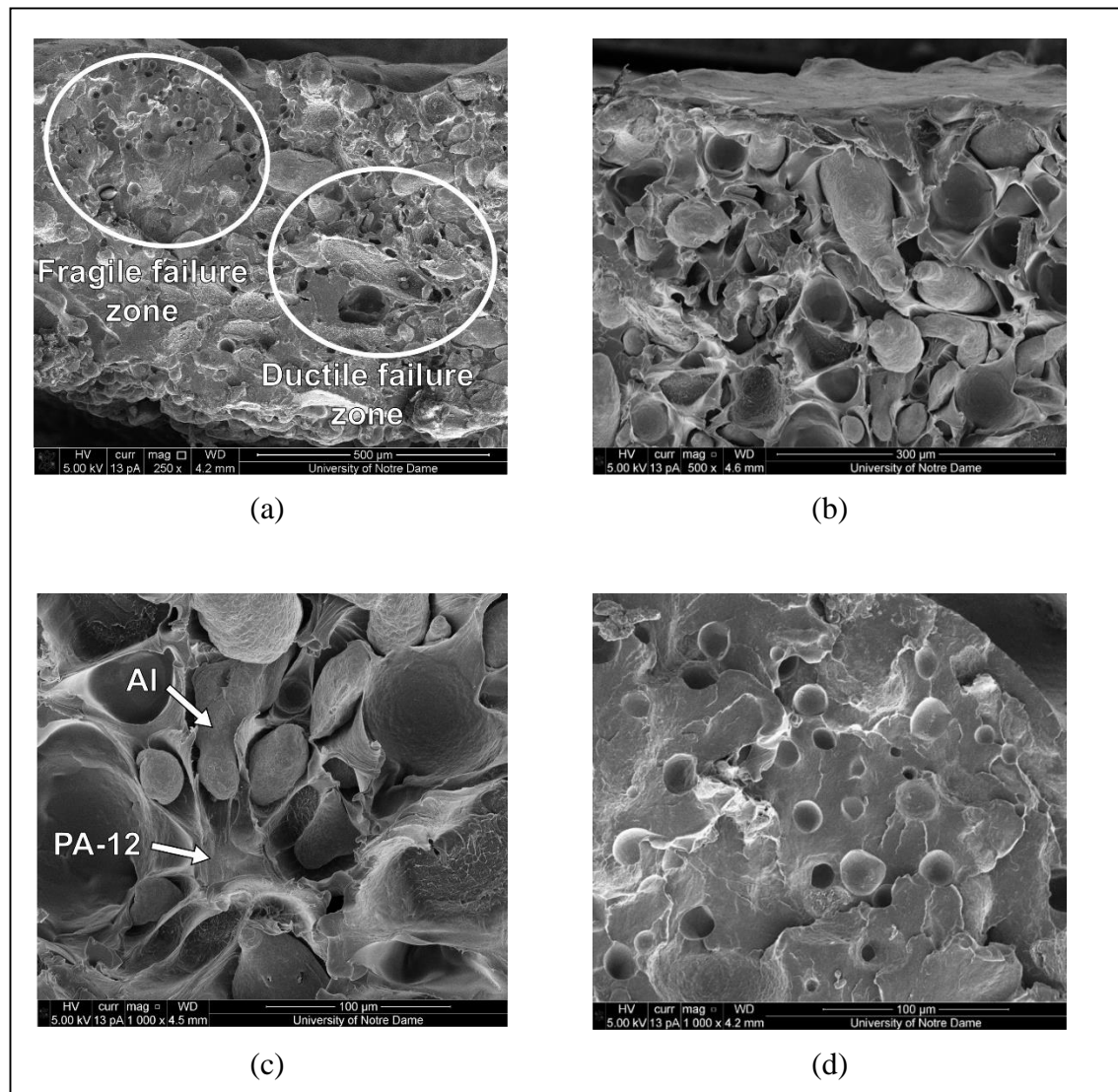


Figure 2-14: Micrographs at the fractured surface. (a) Overall view of a specimen printed at 11 W, 21% oxygen, and 0° showing a ductile and a fragile fracture zones (250x). (b) Top area of a specimen printed at 11 W, 0.5% oxygen, and 0° (500x). (c) Ductile fracture zone at the middle of the specimens of specimen printed at 11 W, 0.5% oxygen, and 0° (1000x). (d) Fragile fracture zone at the top of a specimen printed at 11 W, 21% oxygen, and 0° (1000x).

Three different regions with distinctive characteristics and morphology were recognized on the specimens: a top, a middle, and a bottom region. The top region consists of a thinner layer of polyamide due to the differences in specific weight between the polyamide and

Al particles. The PA-12 is a semicrystalline polymer, and amorphous zones and spherulites were identified on the top surface of the specimens (Figure 2-15). Spherulites are spherical symmetric crystal of polymers. Their formation occurs during the cool down of the polymer by a slowed and controlled recrystallization of the polyamide, which creates the spherulite core by primary nucleation, followed by the radial growth of fibrillar crystals at a constant rate. Frequently, spherulites regions are more densely packed than in the amorphous phase of the polymer; therefore, some mechanical properties like density, tensile strength, and Young's modulus increase in those regions (Carraher, 2003), (Crist & Schultz, 2016). The middle region of the specimens is the most extended area and is formed by Al particles submerged in a polyamide matrix.

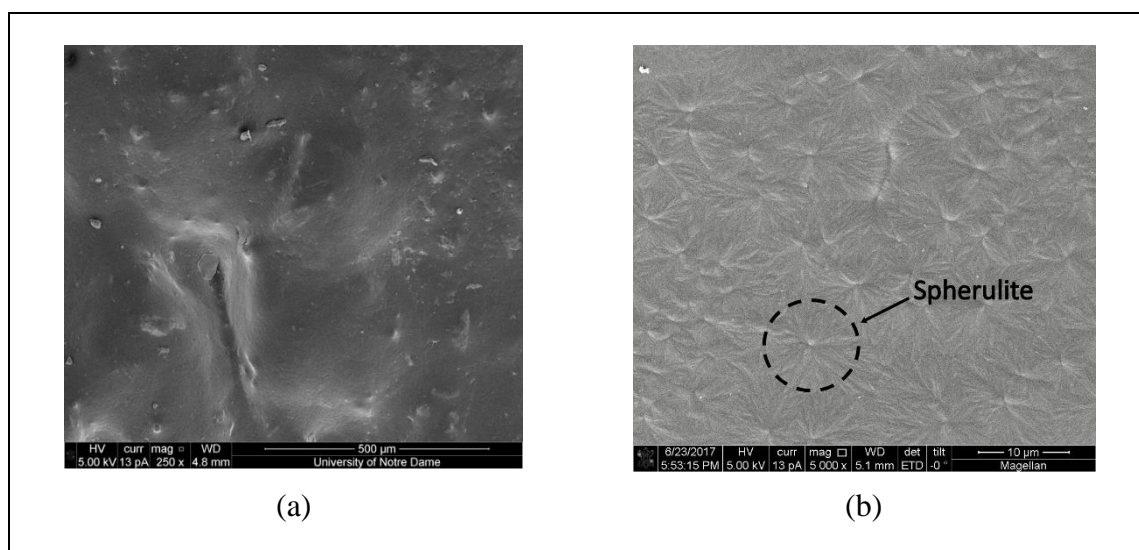


Figure 2-15: Micrographs of the top surface of the specimens. (a) Overall view of a specimen printed at 10 W, 21% oxygen, and 60° (250x). (b) Amplification of the spherulites formed on the polyamide matrix having a diameter near to 10 μm (5000x).

Two different failure zones were identified in this region: a ductile failure zone where Al particles are well distributed, and a fragile failures zone where there is absence of Al particle due to the coagulation of polyamide particles. The ductile failure zones are more common in this region. The stress-strain curves in Figure 2-4 verified that the ductile failure is the predominant mechanism of failure of the specimens. The bottom region is formed by a mixture of Al and polyamide particles adhered to the melted polyamide

matrix (Figure 2-16). The morphology in this region presents a bigger number of voids, higher porosity, and higher surface roughness. The characteristics of this region are explained by the phenomenon of the melt pool, where a lower energy density reaches the bottom of the layer and there is not enough energy to melt the polyamide. Therefore, the polyamide sintered between each other and the powder particles joined to the melted polyamide on the top. Figure 2-17 illustrates an excellent example of an unmelted polyamide particle adhered to the melted polyamide matrix.

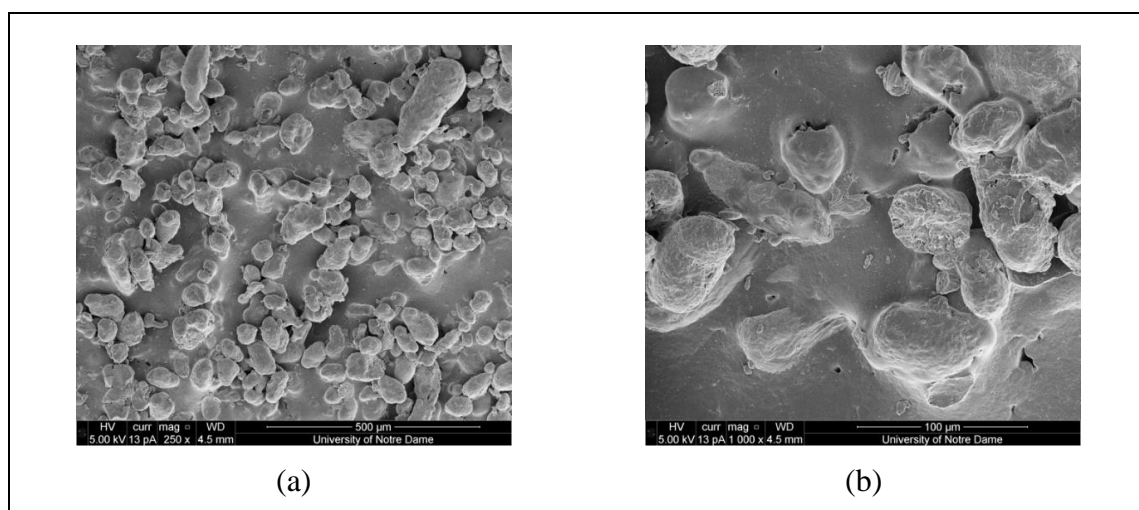


Figure 2-16: Micrographs of the bottom surface of the specimens. (a) Overall view of a specimen printed at 11 W, 21% oxygen, and 60° (250x). (b) Amplification of the image (1000x).

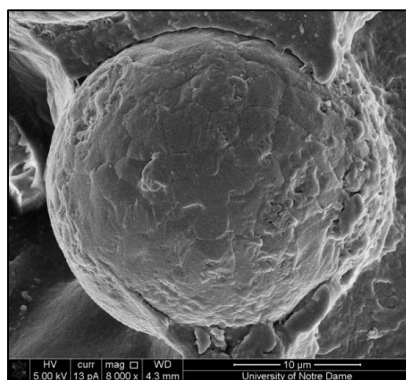


Figure 2-17: Micrograph at the bottom area of the fractured surface. An unmelted PA-12 particle is adhered and surrounded by melted PA-12 (8000x).

2.4.4. Microtomography

A 3D density and geometry phantom evaluation procedure using a MicroCT was used to analyze the internal structure and measure the porosity of one replica of no tensile testing specimens. Figure 2-18 shows the cross-sections analysis of two different specimens printed at different oxygen levels. No significant differences were found for specimens printed at different oxygen levels with the same scanning angle and laser power, which confirms the results from Section 2.5.3. The internal structure of the specimens is revealed in Figure 2-18 and Figure 2-19, where an important amount of voids and pores can be appreciated inside of them. The porosity occurs during the consolidation process. Due to the different size of the particles, gaps between the particles exist. When the polyamide particle is melted, the polyamide starts to flow between the Al particles; however, since the melted polymers have high viscosity and no pressure is applied, not all the gaps are filled, and voids and traps remain in the solid part. It is important to notice that this reduces the effective cross section and the tensile strength of objects. The average porosity of the specimens was 9.8%. Massoli et al., 2007 achieved porosities of 6% for 3-D bars of the same material; therefore, this is another reason why the values of tensile strength and elongation obtained in this research are 45% and 36% lower than the EOS MDS values. Warping had a considerable effect on all the specimens, generating a curved shape that can be noticed in the cross-section images in all the specimens. The melting point of the polyamide is around 176°C; however, the ambient temperature was 20°C and no heating was implemented during the sintering process. Because of this high temperature difference between the bar and the surrounding atmosphere, heat transfer via radiation and convection predominate over conduction, and the top surface of the bar cools down faster than the bottom surface during the solidification process. This generates a significant thermo-gradient across the thickness which is able to warp the specimens.

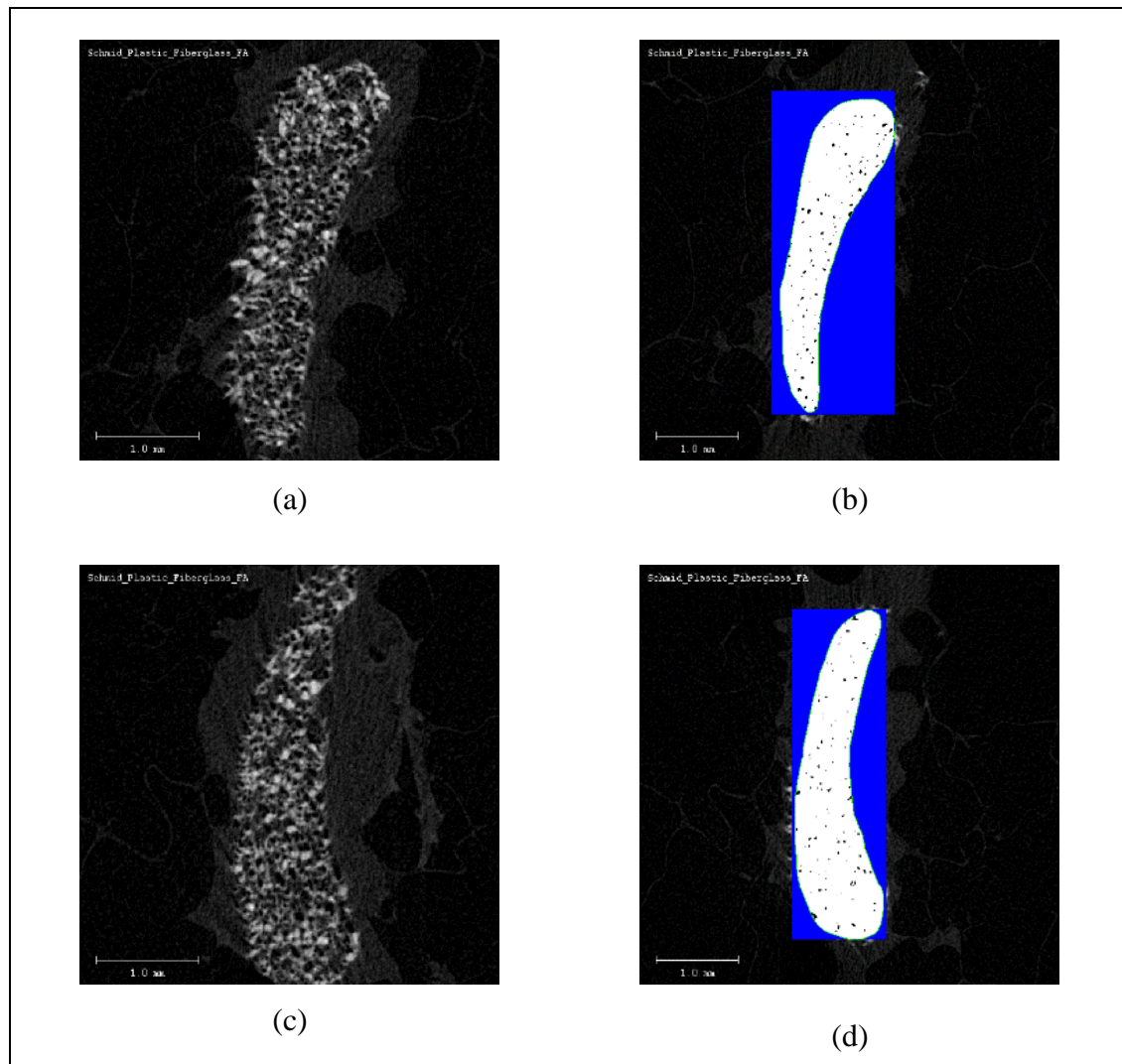


Figure 2-18: Micro CT cross-section images. (a) Specimen printed at 10 W, 21% oxygen, and 60°. (b) Phantom evaluation of the specimen printed at 10 W, 21% oxygen, and 60°. (c) Specimen printed at 10 W, 0.5% oxygen, and 60°. (d) Phantom evaluation of the specimen printed at 10 W, 0.5% oxygen, and 60°.

The path of the laser beam can be noticed on the specimens in Figure 2-19. During the beam scanning process, the melt pool creates a scanning line which is thicker at the middle. This is because of the energy density gradient produced by the focus of the laser beam. Also, a hatch distance is used between each scanning line; consequently, the laser-sintered layer has different thicknesses due to the laser path. Moreover, the different scanning

angles generate distinct paths in the specimens. Using an angle of 0° , horizontal lines across the specimens can be observed, and the thickness through the cross-section is constant. Inclined lines are observed for specimens printed at 45° and 60° , and the thickness of the specimen oscillates through the cross-section according to the inclination of the path lines.

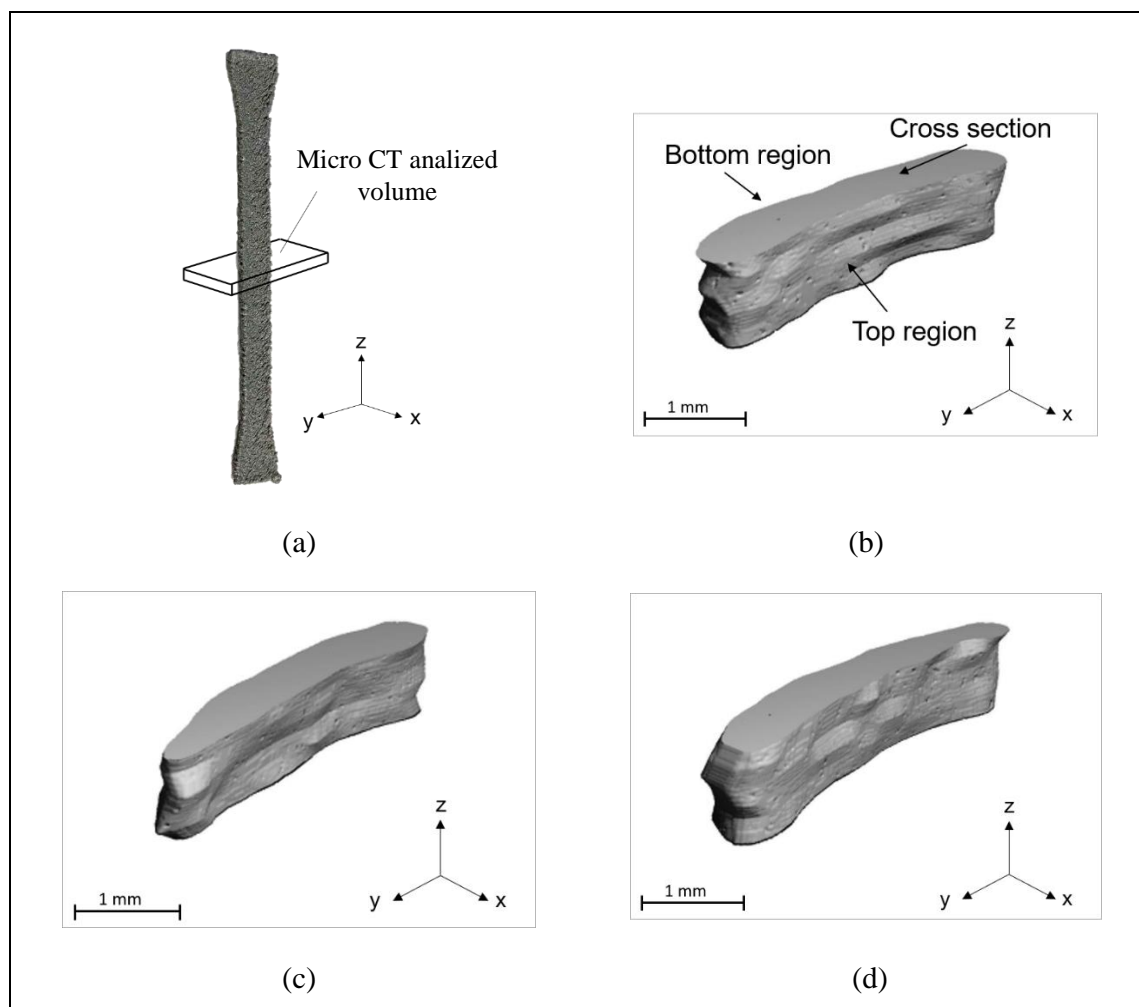


Figure 2-19: 3-D Micro CT images of specimens at 11 W and 0.5% oxygen with different scanning angles. (a) Full specimen. (b) Analyzed volume of a specimen printed at 0° , (c) at 45° , and (d) at 60° .

2.5. Conclusions

In this investigation, aluminum-filled polyamide monolayers specimens were printed by SLS to study the influence of the printed parameters scanning direction, atmospheric oxygen and laser power on the mechanical properties. Furthermore, the morphology and join mechanism of the monolayers were analyzed. In conclusion, the postulated hypotheses was partially correct. The printing SLS parameters scanning angle and laser power have an influence on the UTS, elongation, and layer thickness; however, the oxygen level only has a small effect on the elongation to fracture and on the others properties when combined with laser power or scanning angle.

Increasing the scanning angle achieves better mechanical properties, because of the anisotropy of the SLS printed objects. The scanning angle was modified between 0°, 45°, and 60°, with the last one showed to be the best setting in order to maximize the mechanical properties. These results validate those obtained by Jain et al., 2009 and Sabelle et al., 2018. Nonetheless, the density of the layer did not change for the different scanning angle.

The laser power also showed an important influence on the responses. The highest mechanical properties were measured from the specimens printed with the highest ED (higher laser power), validating previous studies (Caulfield et al., 2007), (Negi et al., 2015), (Sabelle et al., 2018). Also, thicker layers where printed with a higher ED. When the ED increases, the meltpool gets larger, and two competing forces are seen: a polymer degradation versus more molten polyamide mass to resist tensile forces. A higher laser power provided a bigger amount of energy to melt and fused the powder particle, creating thicker layers and specimens with better mechanical properties. In cases when the ED is too high, a higher amount of oxygen degradation will be offset by a larger mass of molten polymer.

The oxygen level only has only a small effect on the elongation to fracture. This means that the oxidation of the polyimide and aluminum does not predominate during the process; nevertheless, it has a small influence on the printed specimens.

Moreover, the scanning angle and oxygen level on their own have no significant effect on the density, and the used range of laser power was not wide enough to cause any effect on

the density. As expected, a correlation between the porosity and the density of the specimen was observed. Higher porosity leads to a lower density.

Finally, a morphology analysis revealed a main internal composite structure formed by filled-reinforcement Al particles submerged in a polyamide matrix, where the failure occurs at the polyamide matrix. When the temperature in the powder rises due to the laser beam scanning, only the polyamide melts because its melting point is much lower than that of the Al. Therefore, the melted polyamide starts to flow filling the gaps between the Al particles and surrounding them, which generates a strong and dense part. Two failure mechanisms were observed. On one hand, when the different particles are well-blended the crack propagations in the polyamide are obstructed by the Al particles, allowing the polyamide matrix to yield, which leads to a ductile fracture. On the other hand, the zones that have polyamide agglomerations and poor amount of Al particles a fragile failure occurs because the cracks propagate freely and easily across that area. These results corroborate the joint mechanisms found by Bassoli et al., 2012 for 3-dimensional bars printed using the same material.

2.6. Further Research

Further work could focus on the effect of the scanning angle and printing orientation on the mechanical properties of the entire bulk, to characterize the anisotropy of the aluminum-filled polyamide 12. This thesis could not analyze the properties 3-D objects because no multilayer SLS was available on the facility. Bassoli et al., 2012 studied and compared mechanical properties and the joint mechanisms of this material printing specimens only at 0°, 45° and 90°; however, considering the results obtained by Jain et al., 2009; Sabelle et al., 2018; and this work, the optimum mechanical properties are reached at 60°.

Commercial SLS machines commonly operate with an inert atmosphere with a powder bed temperature close to the melting point of the polymers to reduce the warping and improve mechanical properties of printed parts. However, this research used an ambient powder bed temperature during the scanning process. Considering that the degradation of polymers in air at high temperature is essentially oxidative in nature, the degradation and

oxidation of the polyamide could be studied to better understand and quantify the influence the oxygen level on the mechanical properties, such as UTS, elongation and density, and the morphology of SLS object. Wudy et al., 2014 showed that the polyamide 12 melt volume and viscosity were reduced by storing the powder under vacuum during the powder coating process; however, our literature review did not found any work related to the influence in other mechanical properties.

REFERENCES

- Bassoli, E., Gatto, A. & Iuliano, L., 2012. Joining mechanisms and mechanical properties of PA composites obtained by selective laser sintering. *Rapid Prototyping Journal*, 18(2), pp. 100-108.
- Bernard, A., Taillandier, G. & Karunakaran, K. P., 2009. Evolutions of rapid product development with rapid manufacturing: concepts and applications. *International Journal of Rapid Manufacturing*, 1(1), pp. 3-18.
- Carraher, C. E., 2003. *Polymer Chemistry*. Sixth Edition ed. New York, NY: Marcel Dekker, Inc.
- Caulfield, B., McHugh, P. E. & Lohfeld, S., 2007. Dependence of mechanical properties of polyamide components on build parameters in the SLS process. *Journal of Materials Processing Technology*, 182(1-3), pp. 477-488.
- Crist, B. & Schultz, J. M., 2016. Polymer spherulites: A critical review. *Progress in Polymer Science*, Volume 56, p. 1–63.
- Eisen, W. B. et al., 1998. *Powder metal technologies and applications*. Novelty, OH (United States): ASM International.
- EOS GmbH, 2012. Alumide data sheet, s.l.: s.n.
- Franco, A., Lanzetta, M. & Romoli, L., 2010. Experimental analysis of selective laser sintering of polyamide powders: An energy perspective. *Journal of Cleaner Production*, 18(16-17), pp. 1722-1730.
- Gibson, I., Rosen, D. W. & Stucker, B., 2015. *Additive manufacturing technologies : 3D printing, rapid prototyping and direct digital manufacturing*. Second ed. New York ; London: Springer.
- Goodridge, R. D., Tuck, C. J. & Hague, R. J. M., 2012. Laser sintering of polyamides and other polymers. *Progress in Materials Science*, 57(2), pp. 229-267.
- Hopkinson, N., Hague, R. & Dickens, P., 2005. *Rapid manufacturing: an industrial revolution for a digital age..* Berlin: Wiley-Blackwell.

- Jain, P., Pandey, P. & Rao, P., 2009. Effect of delay time on part strength in selective laser sintering. *The International Journal of Advanced Manufacturing Technology*, 43(1), pp. 117-126.
- Kalpakjian, S. & Schmid, S., 2014. *Manufacturing Engineering and Technology*. 7th Edition ed. Boston: Pearson.
- Kim, H. et al., 2017. Experimental Study on Mechanical Properties of Single- and Dual-material 3D Printed Products. *Procedia Manufacturing*.
- Kruth, J. P., Levy, G., Klocke, F. & Childs, T. H. C., 2007. Consolidation phenomena in laser and powder-bed based layered manufacturing. *CIRP Annals - Manufacturing Technology*, 56(2), pp. 730-759.
- Kruth, J. P., Wang, X., Laoui, T. & Froyen, L., 2003. Lasers and materials in selective laser sintering. *Assembly Automation*, 23(4), pp. 357-371.
- Kummert, C., Josupeit, S. & Schmid, H.-J., 2017. Thermoplastic Elastomer Part Color as Function of Temperature Histories and Oxygen Atmosphere During Selective Laser Sintering. *Journal of The Minerals, Metals & Materials Society*, 70(3), pp. 425-430.
- Mazzoli, A., Moriconi, G. & Pauri, M. G., 2007. Characterization of an aluminum-filled polyamide powder for applications in selective laser sintering. *Materials & Design*, Volume 28, pp. 993-1000.
- Montgomery, D. C., 2012. *Design and Analysis of Experiments*. Eighth Edition ed. Hoboken, New Jersey: John Wiley & Sons, Inc..
- Negi, S., Dhiman, S. & Sharma, R. K., 2013. Basics, Applications and Future of additive manufacturing technologies: a review. *Journal of Manufacturing Technology Research*, 5(1), pp. 75-96.
- Negi, S., Dhiman, S. & Sharma, R. K., 2014. Basics and applications of rapid prototyping medical models. *Rapid Prototyping Journal*, 20(3), pp. 256-267.
- Negi, S., Dhiman, S. & Sharma, R. K., 2015. Determining the effect of sintering conditions on mechanical properties of laser sintered glass filled polyamide parts using

RSM. Measurement: Journal of the International Measurement Confederation, Volume 68, pp. 205-218.

Negi, S., Sharma, R. K. & Dhiman, S., 2014. Experimental Investigation of SLS Process for Flexural Strength Improvement of PA-3200GF Parts. *Materials and Manufacturing Processes*, 30(5), pp. 644-653.

Roman, P., Gutierrez-zorrilla, J. M. & Vasco, P., 1985. A Quick Method for Determining the Density of Single crystal. *J. Chem Educ*, 62(2), pp. 167-168.

Sabelle, M., Walczak, M. & Ramos-Grez, J., 2018. Scanning pattern angle effect on the resulting properties of selective laser sintered monolayers of Cu-Sn-Ni powder. *Optics and Lasers in Engineering*, Volume 100, pp. 1-8.

Steen, W. M. & Mazumder, J., 2010. *Laser Material Processing*. Fourth ed. London ; Dordrecht ; Heidelberg ; New York: Springer.

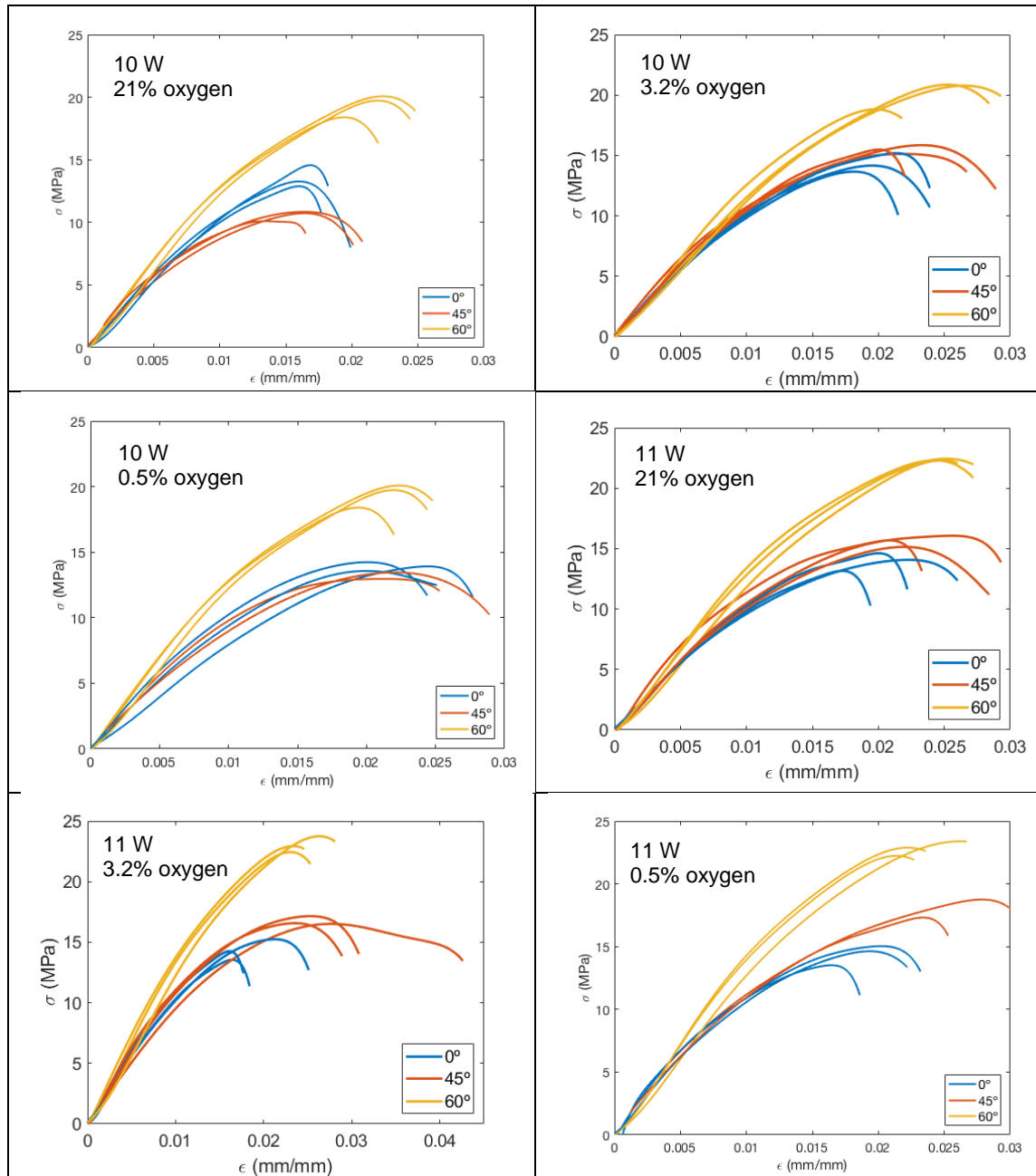
Valkot, E. I. & Chiklis, C. K., 1965. Effects of Thermal Exposure on the Physicochemical Properties of Polyamides. *Journal of Applied Polymer Science*, 9(8), pp. 2855-2877.

Wohler, T., 2001. *Rapid Prototyping & Tooling State of the Industry: Annual Worldwide Progress Report*, Montreal: Wohlers Associates, Inc..

Wudy, K., Drummer, D., Kühnlein, F. & Drexler, M., 2014. Influence of degradation behavior of polyamide 12 powders in laser sintering process on produced parts. *AIP Conference Proceedings*, 1593(1), pp. 691-695.

Zarringhalam, H., Hopkinson, N., Kamperman, N. F. & de Vlieger, J. J., 2006. Effects of processing on microstructure and properties of SLS Nylon 12. *Materials Science and Engineering A*, Volume 435-436, pp. 172-180.

APPENDIX

A. STRESS-STRAIN CURVES FROM TENSILE TESTING

B. DESCRIPTIVE STATISTIC FOR THE RESPONSES.

Table B-1: Results of means and standard deviations (SD) for UTS and elongation.

Angle (°)	Oxygen level (%)	Laser Power (W)	UTS (MPa)		Elongation		Count
			Mean	SD	Mean	SD	
0	0.51	10	19.52	0.763	0.02575	0.001748	3
		11	18.59	1.412	0.02136	0.002440	3
	3.2	10	19.46	1.477	0.0184	0.001305	3
		11	18.77	1.561	0.01682	0.001441	3
	21	10	18.80	1.992	0.01856	0.000988	3
		11	18.79	1.064	0.02259	0.003332	3
45	0.51	10	17.86	0.966	0.02512	0.003916	3
		11	22.36	1.243	0.02662	0.003720	3
	3.2	10	20.74	0.737	0.02062	0.001659	3
		11	20.79	0.702	0.02504	0.002621	3
	21	10	17.42	0.688	0.01912	0.002309	3
		11	20.20	1.182	0.02725	0.002913	3
60	0.51	10	23.69	1.448	0.02378	0.001522	3
		11	24.89	1.589	0.02441	0.002107	3
	3.2	10	23.57	1.232	0.02322	0.003724	3
		11	26.09	1.010	0.02385	0.001810	3
	21	10	25.50	0.882	0.02535	0.003945	3
		11	26.38	0.294	0.02686	0.000681	3
Total Average			21.30	1.125	0.0230	0.00234	54

Table B-2: Results of means and standard deviations (SD) for density and specimen thickness.

Angle (°)	Oxygen level (%)	Laser Power (W)	Density (Kg/m ³)		Thickness (mm)		Count
			Mean	SD	Mean	SD	
0	0.51	10	1332	16.16	0.7027	0.026437	3
		11	1340	10.27	0.7662	0.014665	3
	3.2	10	1313	8.73	0.7197	0.014665	3
		11	1318	13.35	0.7578	0.019400	3
	21	10	1327	13.80	0.7239	0.033601	3
		11	1326	8.81	0.7662	0.019400	3
45	0.51	10	1300	45.35	0.7239	0.000000	3
		11	1343	16.74	0.7620	0.012700	3
	3.2	10	1319	4.34	0.7239	0.012700	3
		11	1307	26.79	0.7916	0.014665	3
	21	10	1339	22.19	0.6138	0.019400	3
		11	1303	31.33	0.7874	0.012700	3
60	0.51	10	1344	14.61	0.7662	0.014665	3
		11	1332	7.62	0.8509	0.033601	3
	3.2	10	1338	7.36	0.8043	0.007332	3
		11	1326	9.7	0.8255	0.033601	3
	21	10	1346	11.83	0.7705	0.019400	3
		11	1353	25.26	0.8255	0.000000	3
Total Average			1328	16.35	0.7601	0.017162	54

Table B-3: Results of the porosity analysis.

Angle (°)	Oxygen level (%)	Laser Power (W)	Porosity (%)	Count
0	0.51	10	9.905	1
		11	10.079	1
	21	10	10.079	1
		11	10.042	1
40	0.51	10	9.243	1
		11	9.73	1
	21	10	9.537	1
		11	10.033	1
60	0.51	10	9.39	1
		11	9.62	1
	21	10	9.905	1
		11	9.574	1
Total Average			9.761	12

C. ANOVA TEST RESIDUALS PLOTS

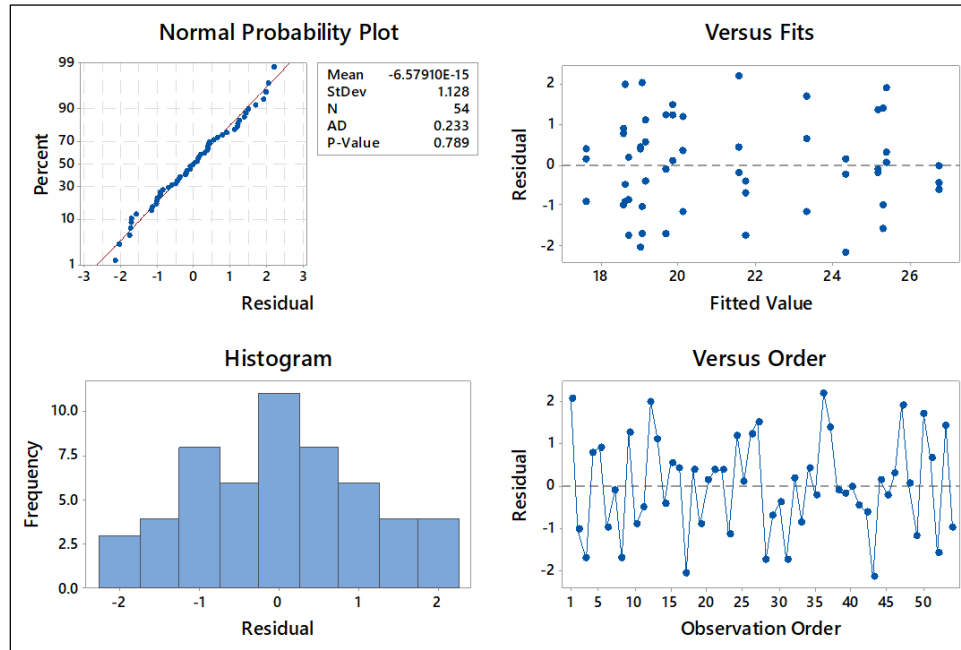


Figure C-1: Residuals plots for ultimate tensile strength.

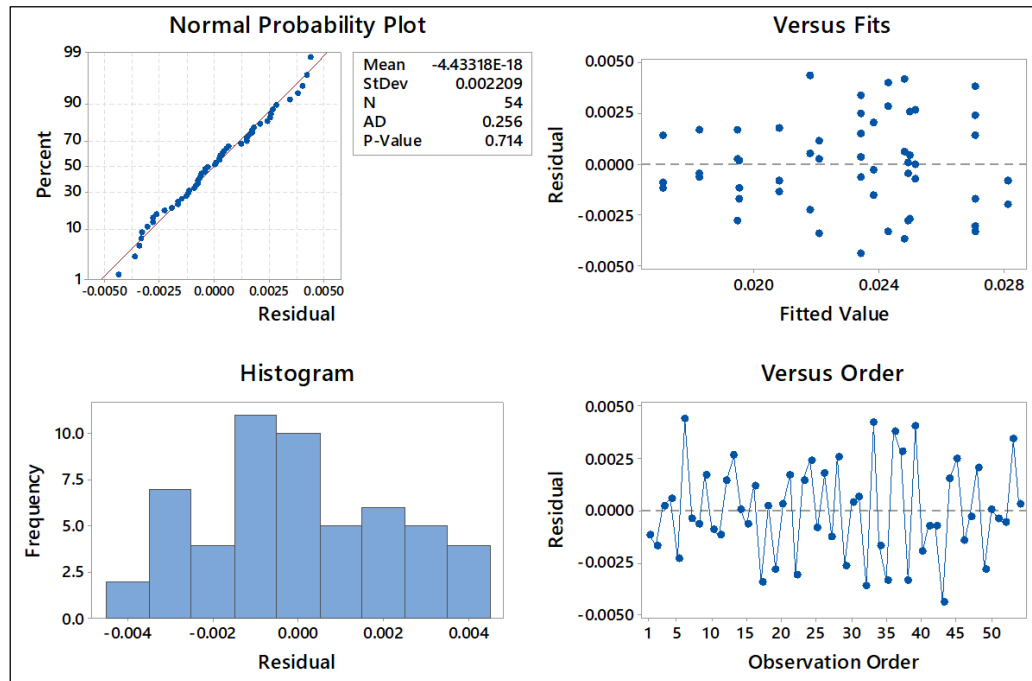


Figure C-2: Residuals plots for elongation.

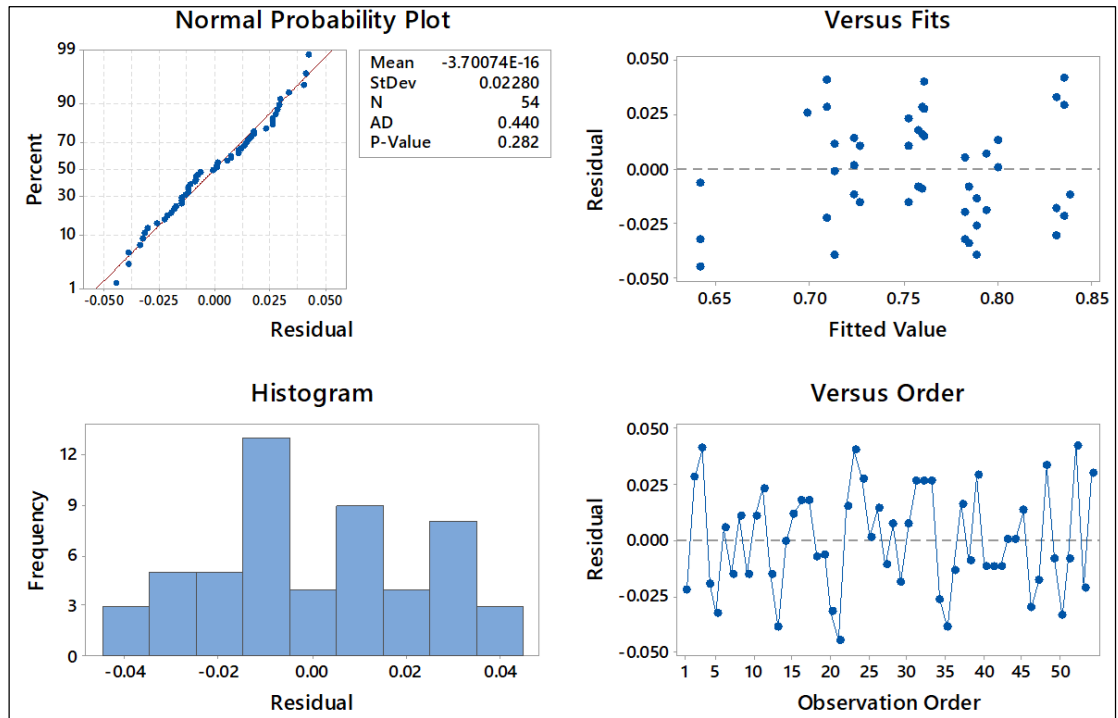


Figure C-3: Residuals plots for specimen thickness.

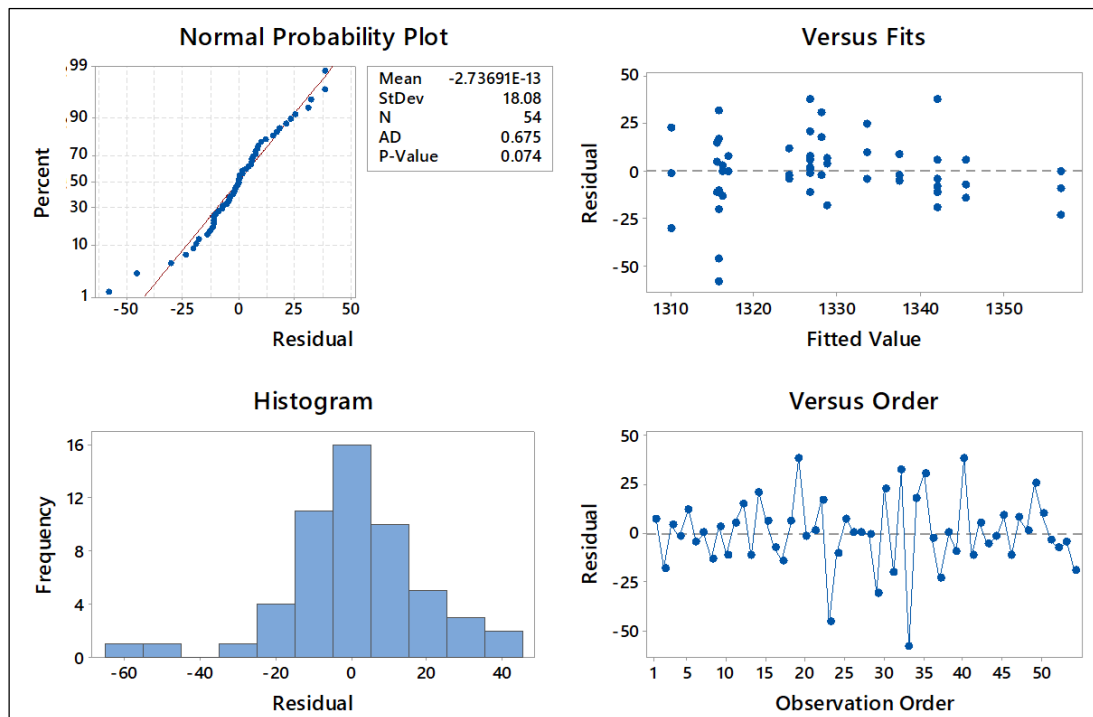


Figure C-4: Residuals plots for density.

D. REGRESION EQUATIONS

$$\begin{aligned}
 \text{UTS (MPa)} = & 21.301 - 2.314 \text{ Angle } (^{\circ})_0 - 1.406 \text{ Angle } (^{\circ})_{45} + 3.720 \text{ Angle } (^{\circ})_{60} \\
 & - 0.150 \text{ Oxygen } (\%)_{0.51} + 0.268 \text{ Oxygen } (\%)_{3.20} - 0.119 \text{ Oxygen } (\%)_{21.00} \\
 & - 0.571 \text{ Laser Power (W)}_{10} + 0.571 \text{ Laser Power (W)}_{11} \\
 & + 0.218 \text{ Angle } (^{\circ}) * \text{Oxygen } (\%)_0 \text{ 0.51} - 0.142 \text{ Angle } (^{\circ}) * \text{Oxygen } (\%)_0 \text{ 3.20} \\
 & - 0.075 \text{ Angle } (^{\circ}) * \text{Oxygen } (\%)_0 \text{ 21.00} + 0.365 \text{ Angle } (^{\circ}) * \text{Oxygen } (\%)_{45} \text{ 0.51} \\
 & + 0.600 \text{ Angle } (^{\circ}) * \text{Oxygen } (\%)_{45} \text{ 3.20} - 0.965 \text{ Angle } (^{\circ}) * \text{Oxygen } (\%)_{45} \text{ 21.00} \\
 & - 0.583 \text{ Angle } (^{\circ}) * \text{Oxygen } (\%)_{60} \text{ 0.51} - 0.458 \text{ Angle } (^{\circ}) * \text{Oxygen } (\%)_{60} \text{ 3.20} \\
 & + 1.040 \text{ Angle } (^{\circ}) * \text{Oxygen } (\%)_{60} \text{ 21.00} + 0.844 \text{ Angle } (^{\circ}) * \text{Laser Power (W)}_0 \text{ 10} \\
 & - 0.844 \text{ Angle } (^{\circ}) * \text{Laser Power (W)}_0 \text{ 11} - 0.650 \text{ Angle } (^{\circ}) * \text{Laser Power (W)}_{45} \text{ 10} \\
 & + 0.650 \text{ Angle } (^{\circ}) * \text{Laser Power (W)}_{45} \text{ 11} - 0.194 \text{ Angle } (^{\circ}) * \text{Laser Power (W)}_{60} \text{ 10} \\
 & + 0.194 \text{ Angle } (^{\circ}) * \text{Laser Power (W)}_{60} \text{ 11} - 0.223 \text{ Oxygen } (\%) * \text{Laser Power (W)}_{0.51} \text{ 10} \\
 & + 0.223 \text{ Oxygen } (\%) * \text{Laser Power (W)}_{0.51} \text{ 11} \\
 & + 0.258 \text{ Oxygen } (\%) * \text{Laser Power (W)}_{3.20} \text{ 10} \\
 & - 0.258 \text{ Oxygen } (\%) * \text{Laser Power (W)}_{3.20} \text{ 11} \\
 & - 0.036 \text{ Oxygen } (\%) * \text{Laser Power (W)}_{21.00} \text{ 10} \\
 & + 0.036 \text{ Oxygen } (\%) * \text{Laser Power (W)}_{21.00} \text{ 11}
 \end{aligned}$$

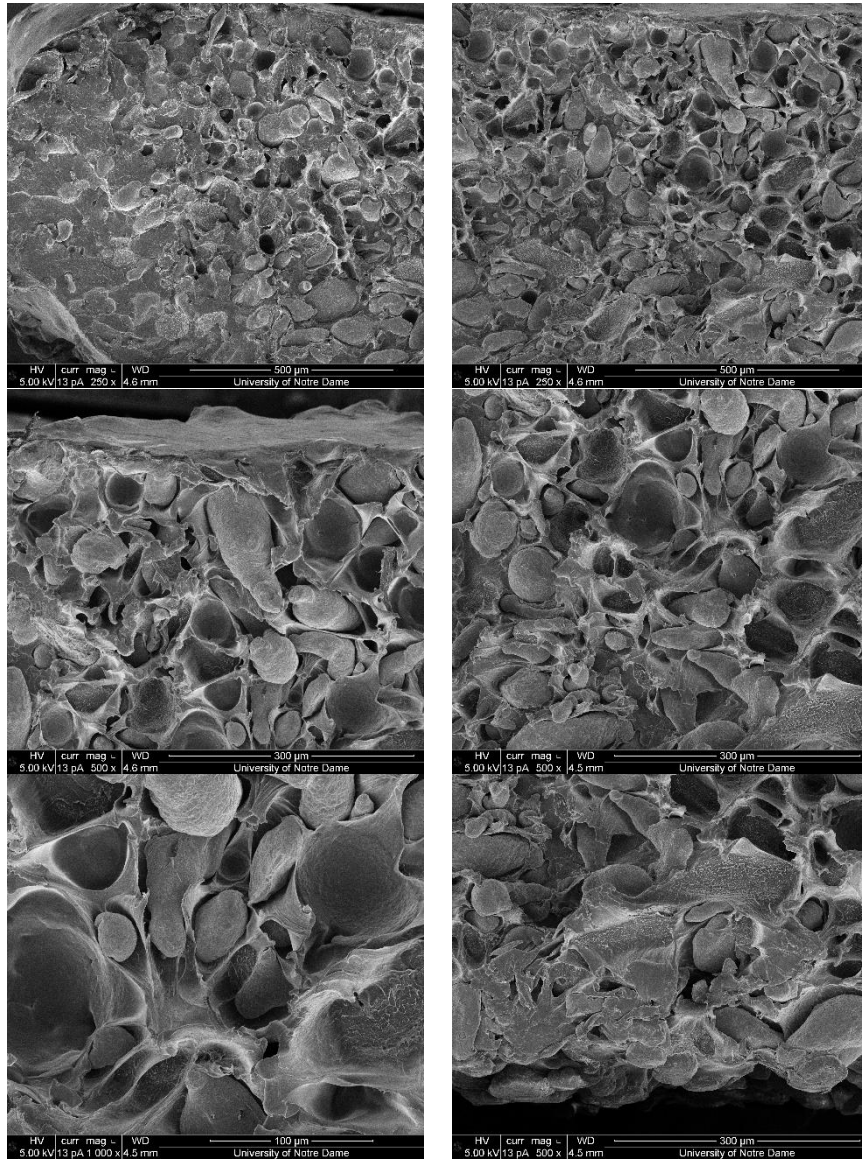
$$\begin{aligned}
 \text{Elongation} = & 0.023041 - 0.002458 \text{ Angle } (^{\circ})_0 + 0.000920 \text{ Angle } (^{\circ})_{45} + 0.001538 \text{ Angle } (^{\circ})_{60} \\
 & + 0.001465 \text{ Oxygen } (\%)_{0.51} - 0.001714 \text{ Oxygen } (\%)_{3.20} \\
 & + 0.000249 \text{ Oxygen } (\%)_{21.00} - 0.000827 \text{ Laser Power (W)}_{10} \\
 & + 0.000827 \text{ Laser Power (W)}_{11} + 0.001510 \text{ Angle } (^{\circ}) * \text{Oxygen } (\%)_0 \text{ 0.51} \\
 & - 0.001255 \text{ Angle } (^{\circ}) * \text{Oxygen } (\%)_0 \text{ 3.20} - 0.000255 \text{ Angle } (^{\circ}) * \text{Oxygen } (\%)_0 \text{ 21.00} \\
 & + 0.000442 \text{ Angle } (^{\circ}) * \text{Oxygen } (\%)_{45} \text{ 0.51} + 0.000581 \text{ Angle } (^{\circ}) * \text{Oxygen } (\%)_{45} \text{ 3.20} \\
 & - 0.001023 \text{ Angle } (^{\circ}) * \text{Oxygen } (\%)_{45} \text{ 21.00} - 0.001952 \text{ Angle } (^{\circ}) * \text{Oxygen } (\%)_{60} \text{ 0.51} \\
 & + 0.000674 \text{ Angle } (^{\circ}) * \text{Oxygen } (\%)_{60} \text{ 3.20} + 0.001278 \text{ Angle } (^{\circ}) * \text{Oxygen } (\%)_{60} \text{ 21.00} \\
 & + 0.001149 \text{ Angle } (^{\circ}) * \text{Laser Power (W)}_0 \text{ 10} - 0.001149 \text{ Angle } (^{\circ}) * \text{Laser Power (W)}_0 \text{ 11} \\
 & - 0.001515 \text{ Angle } (^{\circ}) * \text{Laser Power (W)}_{45} \text{ 10} \\
 & + 0.001515 \text{ Angle } (^{\circ}) * \text{Laser Power (W)}_{45} \text{ 11} \\
 & + 0.000366 \text{ Angle } (^{\circ}) * \text{Laser Power (W)}_{60} \text{ 10} \\
 & - 0.000366 \text{ Angle } (^{\circ}) * \text{Laser Power (W)}_{60} \text{ 11} \\
 & + 0.001202 \text{ Oxygen } (\%) * \text{Laser Power (W)}_{0.51} \text{ 10} \\
 & - 0.001202 \text{ Oxygen } (\%) * \text{Laser Power (W)}_{0.51} \text{ 11} \\
 & + 0.000247 \text{ Oxygen } (\%) * \text{Laser Power (W)}_{3.20} \text{ 10} \\
 & - 0.000247 \text{ Oxygen } (\%) * \text{Laser Power (W)}_{3.20} \text{ 11} \\
 & - 0.001449 \text{ Oxygen } (\%) * \text{Laser Power (W)}_{21.00} \text{ 10} \\
 & + 0.001449 \text{ Oxygen } (\%) * \text{Laser Power (W)}_{21.00} \text{ 11}
 \end{aligned}$$

$$\begin{aligned}
 \text{Thickness (mm)} = & 0.76012 - 0.02070 \text{ Angle } (^{\circ})_0 - 0.02634 \text{ Angle } (^{\circ})_{45} + 0.04704 \text{ Angle } (^{\circ})_{60} \\
 & + 0.00188 \text{ Oxygen } (\%)_{0.51} + 0.01035 \text{ Oxygen } (\%)_{3.20} \\
 & - 0.01223 \text{ Oxygen } (\%)_{21.00} - 0.03246 \text{ Laser Power (W)}_{10} \\
 & + 0.03246 \text{ Laser Power (W)}_{11} - 0.00682 \text{ Angle } (^{\circ}) * \text{Oxygen } (\%)_0 \text{ 0.51} \\
 & - 0.01105 \text{ Angle } (^{\circ}) * \text{Oxygen } (\%)_0 \text{ 3.20} + 0.01787 \text{ Angle } (^{\circ}) * \text{Oxygen } (\%)_0 \text{ 21.00} \\
 & + 0.00729 \text{ Angle } (^{\circ}) * \text{Oxygen } (\%)_{45} \text{ 0.51} + 0.01364 \text{ Angle } (^{\circ}) * \text{Oxygen } (\%)_{45} \text{ 3.20} \\
 & - 0.02093 \text{ Angle } (^{\circ}) * \text{Oxygen } (\%)_{45} \text{ 21.00} \\
 & - 0.00047 \text{ Angle } (^{\circ}) * \text{Oxygen } (\%)_{60} \text{ 0.51} - 0.00259 \text{ Angle } (^{\circ}) * \text{Oxygen } (\%)_{60} \text{ 3.20} \\
 & + 0.00306 \text{ Angle } (^{\circ}) * \text{Oxygen } (\%)_{60} \text{ 21.00} \\
 & + 0.00847 \text{ Angle } (^{\circ}) * \text{Laser Power (W)}_0 \text{ 10} \\
 & - 0.00847 \text{ Angle } (^{\circ}) * \text{Laser Power (W)}_0 \text{ 11} \\
 & - 0.01411 \text{ Angle } (^{\circ}) * \text{Laser Power (W)}_{45} \text{ 10} \\
 & + 0.01411 \text{ Angle } (^{\circ}) * \text{Laser Power (W)}_{45} \text{ 11} \\
 & + 0.00564 \text{ Angle } (^{\circ}) * \text{Laser Power (W)}_{60} \text{ 10} \\
 & - 0.00564 \text{ Angle } (^{\circ}) * \text{Laser Power (W)}_{60} \text{ 11} \\
 & + 0.00141 \text{ Oxygen } (\%) * \text{Laser Power (W)}_{0.51} \text{ 10} \\
 & - 0.00141 \text{ Oxygen } (\%) * \text{Laser Power (W)}_{0.51} \text{ 11} \\
 & + 0.01129 \text{ Oxygen } (\%) * \text{Laser Power (W)}_{3.20} \text{ 10} \\
 & - 0.01129 \text{ Oxygen } (\%) * \text{Laser Power (W)}_{3.20} \text{ 11} \\
 & - 0.01270 \text{ Oxygen } (\%) * \text{Laser Power (W)}_{21.00} \text{ 10} \\
 & + 0.01270 \text{ Oxygen } (\%) * \text{Laser Power (W)}_{21.00} \text{ 11}
 \end{aligned}$$

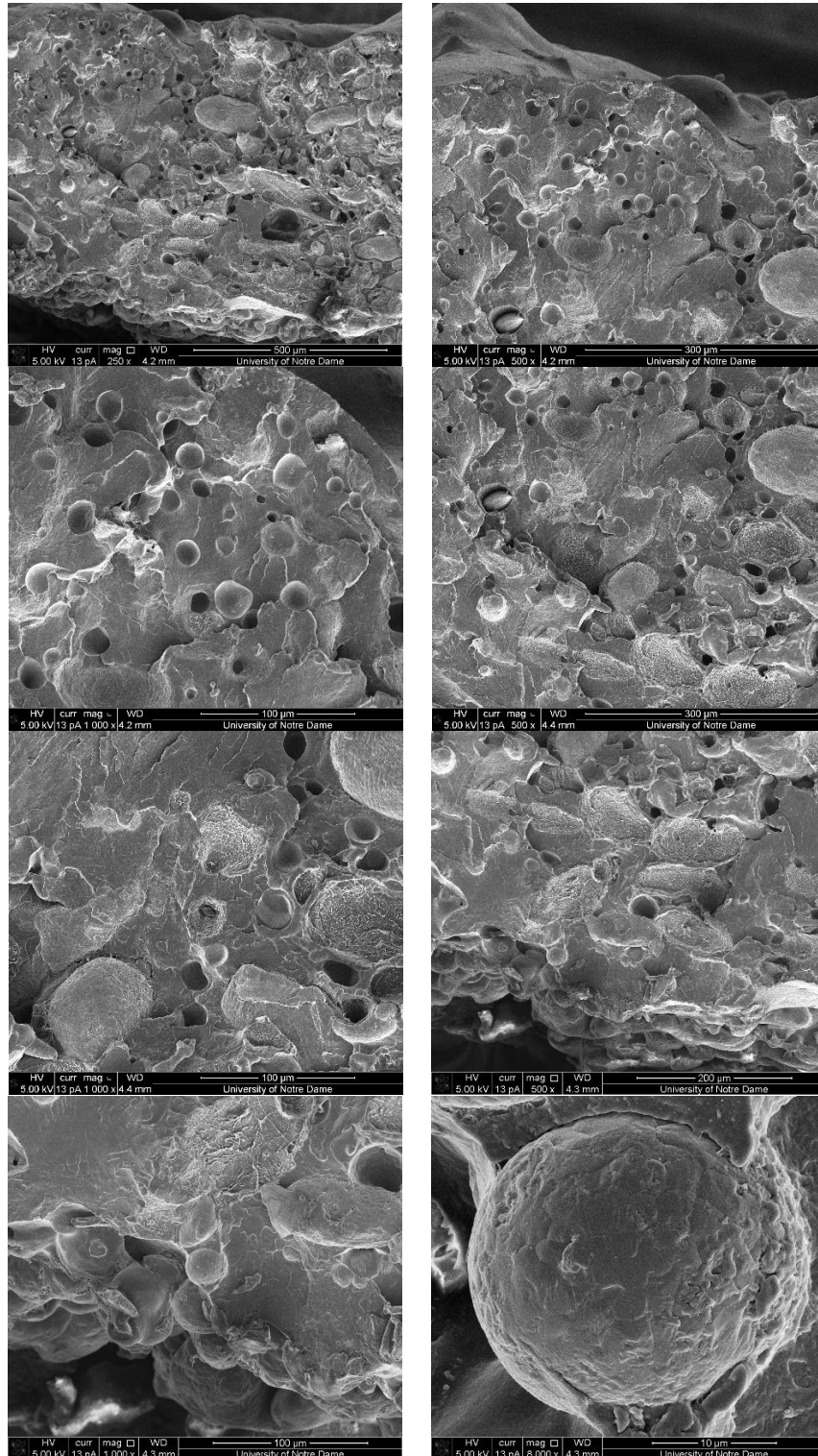
$$\begin{aligned}
\text{Density (Kg/m3)} = & 1328.08 - 2.12 \text{ Angle (°)}_0 - 9.36 \text{ Angle (°)}_{45} + 11.48 \text{ Angle (°)}_{60} \\
& + 3.65 \text{ Oxygen (\%)}_{0.51} - 7.76 \text{ Oxygen (\%)}_{3.20} + 4.11 \text{ Oxygen (\%)}_{21.00} \\
& + 0.49 \text{ Laser Power (W)}_{10} - 0.49 \text{ Laser Power (W)}_{11} \\
& + 6.24 \text{ Angle (°)} * \text{Oxygen (\%)}_0 0.51 - 2.49 \text{ Angle (°)} * \text{Oxygen (\%)}_0 3.20 \\
& - 3.75 \text{ Angle (°)} * \text{Oxygen (\%)}_0 21.00 - 0.64 \text{ Angle (°)} * \text{Oxygen (\%)}_{45} 0.51 \\
& + 2.41 \text{ Angle (°)} * \text{Oxygen (\%)}_{45} 3.20 - 1.77 \text{ Angle (°)} * \text{Oxygen (\%)}_{45} 21.00 \\
& - 5.60 \text{ Angle (°)} * \text{Oxygen (\%)}_{60} 0.51 + 0.08 \text{ Angle (°)} * \text{Oxygen (\%)}_{60} 3.20 \\
& + 5.52 \text{ Angle (°)} * \text{Oxygen (\%)}_{60} 21.00 - 2.73 \text{ Angle (°)} * \text{Laser Power (W)}_0 10 \\
& + 2.73 \text{ Angle (°)} * \text{Laser Power (W)}_0 11 + 0.40 \text{ Angle (°)} * \text{Laser Power (W)}_{45} \\
& 10 - 0.40 \text{ Angle (°)} * \text{Laser Power (W)}_{45} 11 \\
& + 2.33 \text{ Angle (°)} * \text{Laser Power (W)}_{60} 10 - 2.33 \text{ Angle (°)} * \text{Laser Power (W)}_{60} \\
& 11 - 7.09 \text{ Oxygen (\%)} * \text{Laser Power (W)}_{0.51} 10 \\
& + 7.09 \text{ Oxygen (\%)} * \text{Laser Power (W)}_{0.51} 11 \\
& + 2.56 \text{ Oxygen (\%)} * \text{Laser Power (W)}_{3.20} 10 \\
& - 2.56 \text{ Oxygen (\%)} * \text{Laser Power (W)}_{3.20} 11 \\
& + 4.53 \text{ Oxygen (\%)} * \text{Laser Power (W)}_{21.00} 10 \\
& - 4.53 \text{ Oxygen (\%)} * \text{Laser Power (W)}_{21.00} 11
\end{aligned}$$

E. SEM MICROGRAPHS

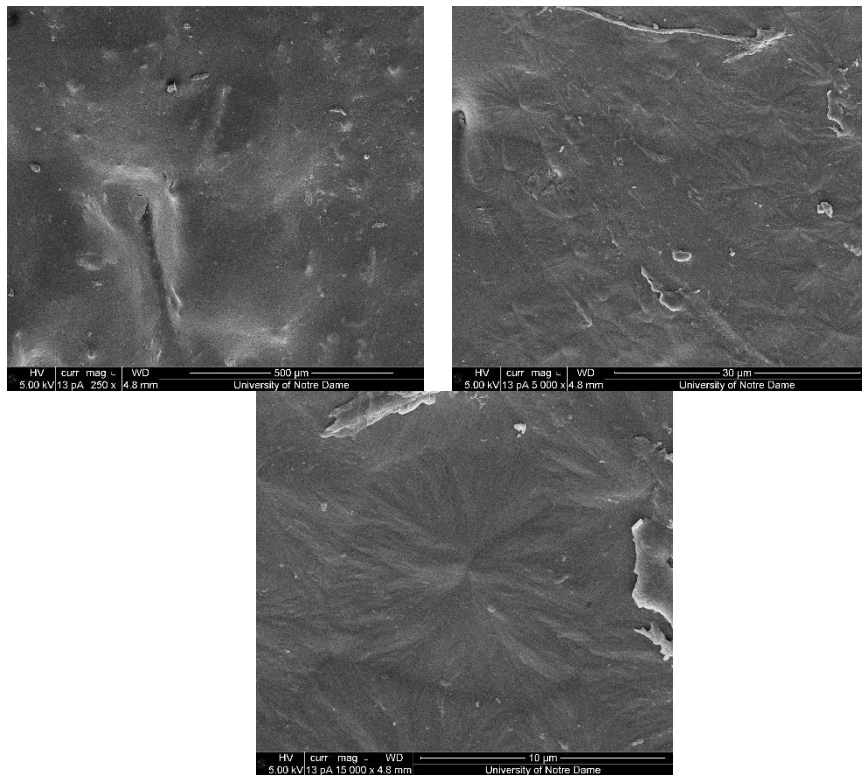
Micrographs at the cross section fractured surface of a specimen printed at 11 W, scanning angle of 0°, and 0.5% of oxygen level:



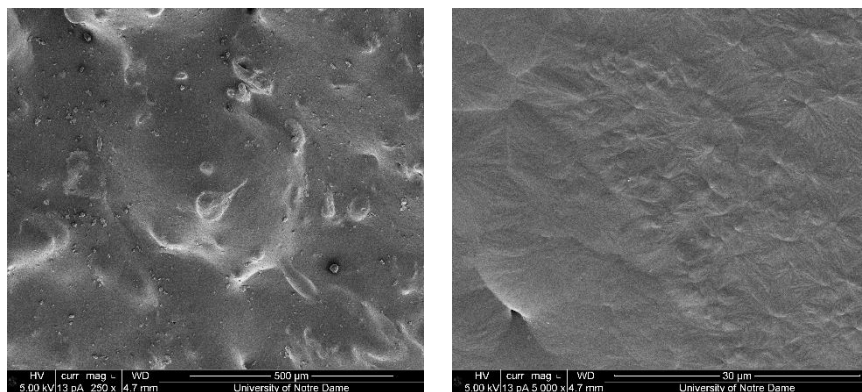
Micrographs at the cross section fractured surface of a specimen printed at 11 W, scanning angle of 0°, and 21% of oxygen level:



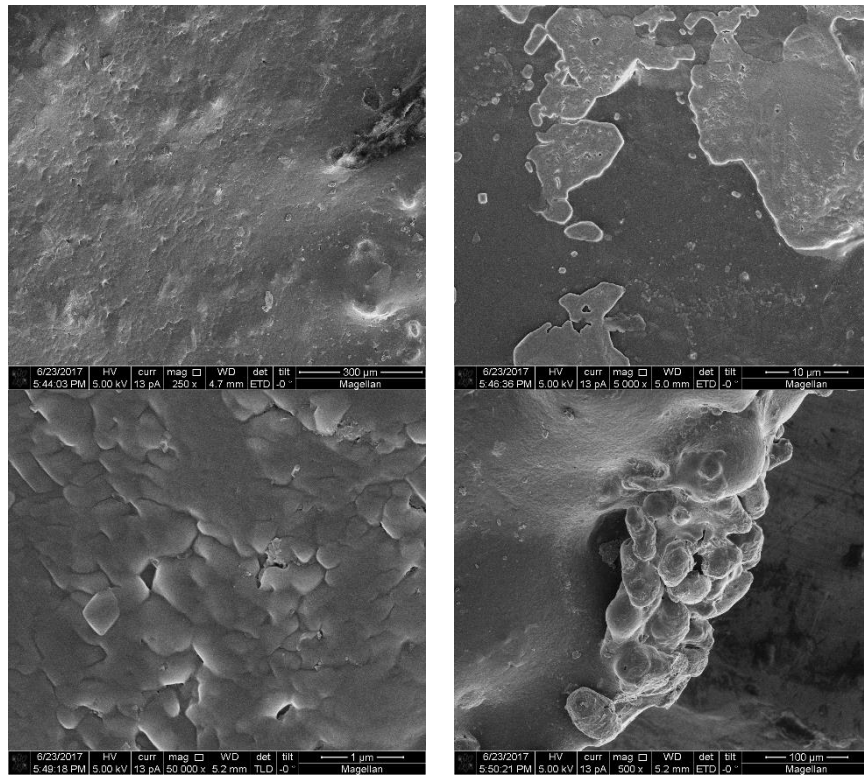
Micrographs at the top surface of a specimen printed at 10 W, scanning angle of 60°, and 21% of oxygen level:



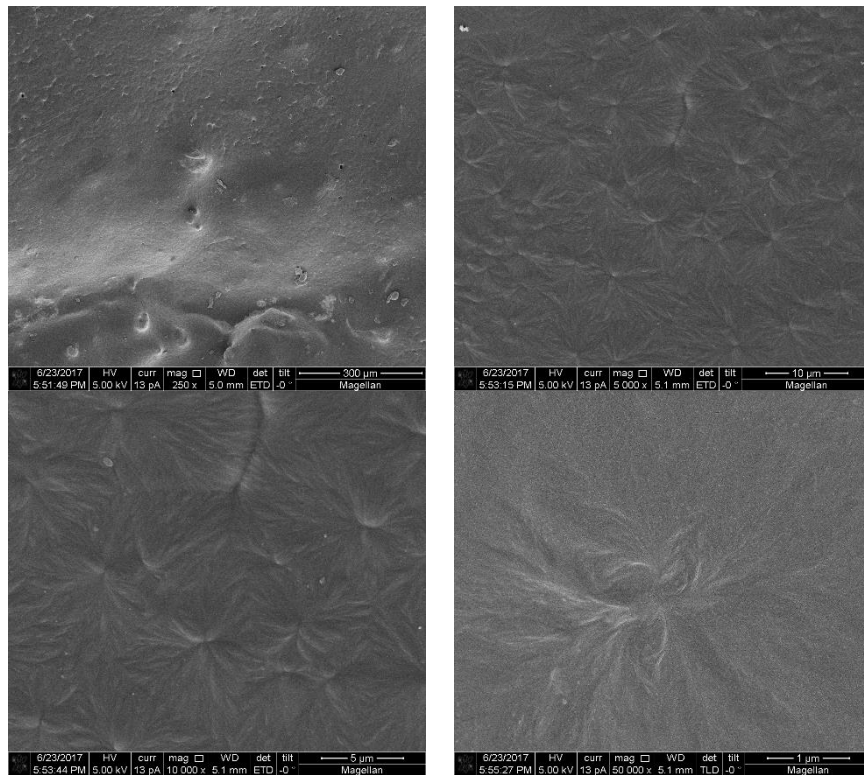
Micrographs at the top surface of a specimen printed at 10 W, scanning angle of 60°, and 0.5% of oxygen level:



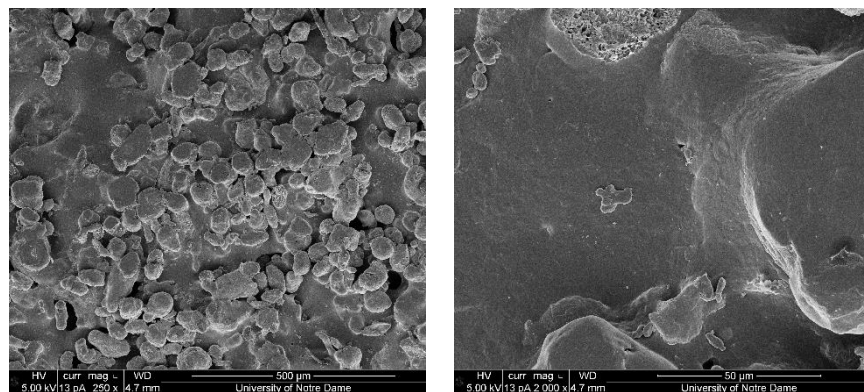
Micrographs at the top surface of a specimen printed at 11 W, scanning angle of 60°, and 21% of oxygen level:



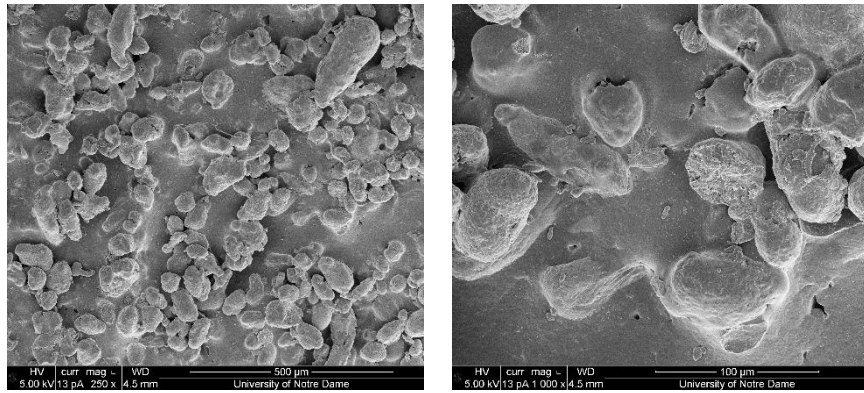
Micrographs at the top surface of a specimen printed at 11 W, scanning angle of 60°, and 0.5% of oxygen level.



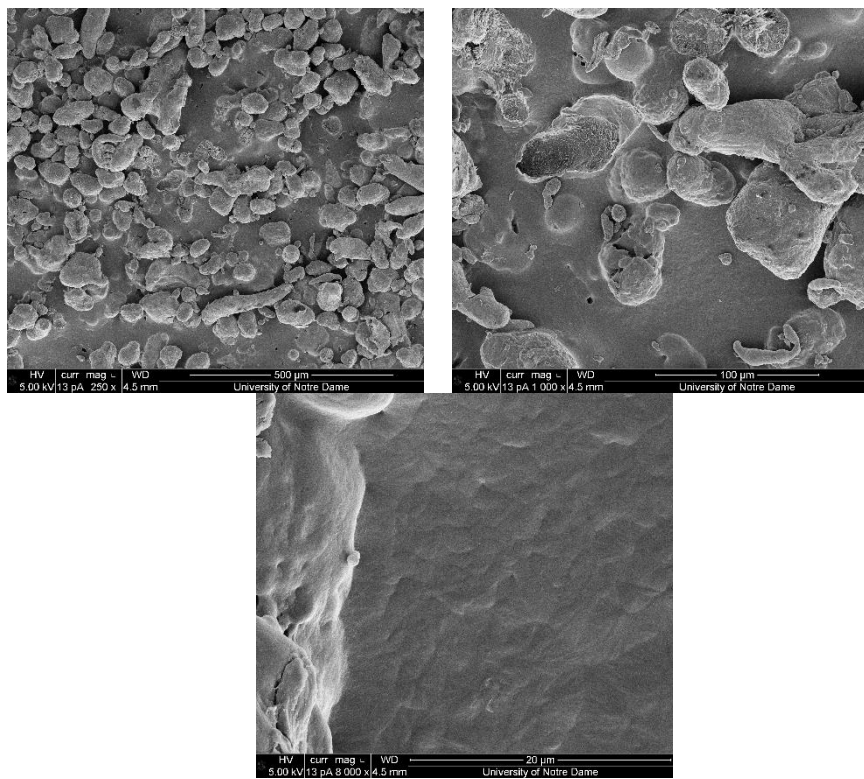
Micrographs at the bottom surface of a specimen printed at 10 W, scanning angle of 60°, and 21% of oxygen level.



Micrographs at the bottom surface of a specimen printed at 11 W, scanning angle of 60°, and 21% of oxygen level.



Micrographs at the bottom surface of a specimen printed at 11 W, scanning angle of 60°, and 0.5% of oxygen level.



F. MICRO CT ANALYSIS

Micro CT cross-section images (left) and phantom evaluation analysis (right) for all no tensile testing specimens, printed at different scanning angles (SA), laser power (LP), and oxygen level (OL):

